Chapter 10
Solar Cell Applications of π-Conjugated Molecules

Kouki Akaike and Kaname Kanai

Abstract Because organic molecules possessing extended π-conjugation show strong absorption in the visible region of the solar spectrum, they have been used as dyes in solid-state photovoltaic devices known as organic solar cells (OSCs). The power-conversion efficiency of tandem OSCs already reportedly exceeds 17% by processing state-of-the-art polymer donors and non-fullerene acceptors from their mixed solution, but this efficiency is still far below that of silicon-based solar cells ($\sim$25%). Deep understanding of the fundamental aspects of OSC operation, such as the mechanism for free-charge generation and the interfacial electronic and morphological properties, is now recognized as being vital to establishing well-defined guidelines for designing material interfaces and device structures and for improving the performance of OSCs. In this chapter, we give a brief historical review of solar cells and the operational mechanism of OSCs, as well as recent developments of new donors, acceptors, and interface modifiers. We then give a thorough explanation of the electronic structure of photoactive π-conjugated molecules and their interfaces used in OSCs based on recent studies, with links to OSC performance.

Keywords Organic photovoltaics · Organic semiconductors · Molecular design · Interfaces · Electronic structure

K. Akaike (✉)
Nanomaterials Research Institute, National Institute of Advanced Industrial Science and Technology, Tsukuba, Japan
e-mail: kouki.akaike@aist.go.jp

K. Kanai
Department of Physics, Faculty of Science and Technology, Tokyo University of Science, Tokyo, Japan

10.1 Introduction

Fossil fuels have been consumed abundantly to produce the energy that has been essential for developing and sustaining human civilization. However, with global economic growth and improved quality of life, electricity demand is increasing steadily, as are concerns about how much fossil fuel remains. This urgent problem regarding the natural environment has prompted researchers to develop devices that can produce energy in ways that are environmentally friendly, renewable, and sustainable. The solar cell is a promising energy device that utilizes the photovoltaic effect to convert the energy of sunlight into electrical energy. As most readers already recognize, silicon-based solar cells are well-established in the market; they can be found to be mounted on buildings and houses or placed on the ground to generate electricity collectively from an abundant natural resource. The discovery of the photovoltaic effect can be traced back to Becquerel's work on liquid electrolytes in 1839 [1]. In 1954, Chapin et al. at Bell Laboratory reported a *p-n* junction silicon solar cell with a power-conversion efficiency of 6% [2]. Since then, many different semiconducting materials have been used as the photoactive layer (or simply the active layer) in solar cells.

Let us describe briefly the solar spectral irradiance distribution collected by the National Renewable Energy Laboratory (NREL) [3] (Fig. 10.1a). Outside the Earth's atmosphere (extraterrestrial), the solar spectrum is approximated as the irradiance emitted from a black body at 5800 K with a peak at $\sim$500 nm. However, we have to consider the influence of the atmosphere when considering the solar irradiance that reaches the Earth. This is because photons with higher energies
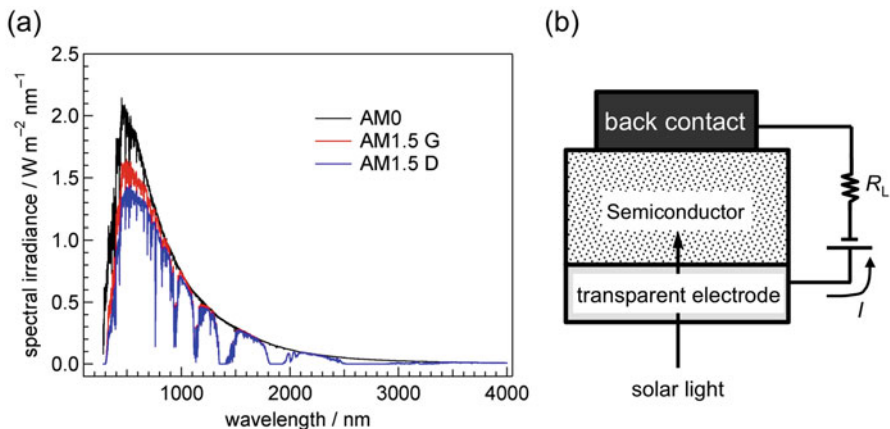

Fig. 10.1 (**a**) Solar spectral irradiance distribution. G and D after AM1.5 denote global total spectral irradiance and direct normal spectral irradiance, respectively. AM1.5 G includes the surrounding ground and the blue sky. AM1.5 D includes the direct beam from the sun plus the circumsolar component in a 2.5° disk around the sun. (**b**) Schematic structure of solar cell with load R_L and photocurrent I

(i.e., ultraviolet and blue light) are scattered (Rayleigh scattering) and absorbed by water vapor in the atmosphere, thereby reducing the spectral irradiance that reaches the Earth.

To express the atmospheric influence on solar spectra, we use the air mass (AM) expressed by $1/\cos\theta$, where θ is the zenith angle. The AM denotes the volume of air that solar light travels through before reaching the Earth's surface. An angle of $\theta = 48.19°$ gives an AM of 1.5, which is often denoted as AM1.5. For the standard characterization of solar cells, a light source with an energy of 100 mW cm^{-2} is used that is filtered to match the AM1.5 spectral irradiance (Fig. 10.1a). The semiconducting material used in the solar cell must absorb photons corresponding to the AM1.5 irradiance, ideally up to the near-infrared range, in order to produce more photocurrent from sunlight. The absorption ability of the material is related to its optical band gap ($E_{g,opt}$), which is defined as the energy difference between the valence band and the conduction band. For organic molecules, $E_{g,opt}$ is determined by the energy difference between the highest occupied molecular orbital (HOMO) and the lowest unoccupied molecular orbital (LUMO) and by the exciton binding energy due to the low dielectric constant of organic molecules. Photons with energies greater than $E_{g,opt}$ can excite electron from occupied states into unoccupied states. The smaller $E_{g,opt}$ is, the more photons are absorbed from sunlight. For example, Si has a (indirect) band gap of 1.1 eV, which enables photoabsorption at wavelengths below 1200 nm.

The basic structure of a solar cell is a semiconductor (e.g., Si, GaAs) sandwiched between a transparent electrode [e.g., indium tin oxide (ITO)] and a back contact such as Al (Fig. 10.1b). Free carriers generated upon photoabsorption within the semiconductor photoactive layer result in a photocurrent I, and electrical energy is extracted from a load R_L.

Among the various types of solar cell, we focus here on organic solar cells (OSCs) that are based on π-conjugated small molecules and polymers. OSCs have attracted tremendous amounts of interest, and the current record for power-conversion efficiency is held by a multi-junction (tandem) OSC at over 17% [4]. Compared to inorganic semiconductors, hydrocarbon solids tend to be "soft"

Fig. 10.2 (**a**) Photograph of the standing meniscus during slot-die coating of the active layer of an OSC comprising many very tightly spaced stripes. (**b**) A total of 48 stripes are coated simultaneously. (**c**) Knife coating with an open ink reservoir and a manual feed hose. (Reprinted with permission from Ref. [5])

because the molecules aggregate in the solid state as a result of van der Waals intermolecular interaction (mainly the London dispersion force). The mechanical softness of organic semiconductors allows us to fabricate flexible solar cells on plastic substrates that could be attached even to curved walls and windows and to fabricate such flexible OSCs by means of the roll-to-roll processes (Fig. 10.2) [5]. In addition, thanks to advanced organic synthesis, it is possible to functionalize organic semiconductors in order to dissolve them into common solvents. Using solution processes such as dip coating and spin coating to fabricate OSCs can therefore reduce the associated production costs, resulting in a shorter payback time (i.e., the time required to recoup the initial investment).

The first reported use of organic molecules for photoelectric conversion was in 1906 [6]. Subsequently, Prof. Inokuchi referred to π-conjugated molecules that show electrical conduction as an *organic semiconductor* after he found photoconduction in thin films of violanthrone [7, 8]. Since then, the potential of organic semiconductors as electronic components in devices such as light-emitting diodes [9, 10] has been explored rigorously. In the early stages of OSC research, porphyrins, phthalocyanines, and merocyanines were used as the active layer in Schottky-barrier OSCs [11]. However, in spite of their high absorption coefficients in the visible range of the solar spectrum and the high crystallinity of their vacuum-deposited films, power-conversion efficiency of OSCs based on these molecules was limited to 0.7% at most in the early 1980s [11]. This was despite efforts to increase carrier concentration and thus conductivity by doping with oxygen and gaseous halogens, for example [11].

However, C. W. Tang of Kodak achieved the efficiency of 1.0% for an OSC with a bilayer structure consisting of copper phthalocyanine (CuPc; molecular structure is shown in Fig. 10.3) and a perylene derivative [12–14]. This prompted worldwide interest in the synthesis of photoactive materials, the optimization of device configurations, and interface engineering to develop more efficient OSCs.

Figure 10.3 shows representative organic semiconductors for the photoactive layer of an OSC. Before use, the semiconducting organic molecules have to be purified sufficiently because material purity severely influences the fill factor and hence the overall device efficiency [15–17]. The abbreviation for each molecule is given in the figure caption. For Schottky-barrier OSCs, one organic semiconductor is used as the sole component for photoelectric conversion and is sandwiched between the anode (hole-collecting electrode) and cathode (electron-collecting electrode) (Fig. 10.4a). By the late 1980s, most OSC devices were based on this simple structure. At that time, the performance based solely on phthalocyanine and merocyanine was poor, as already mentioned. However, fullerenes and SubPc have recently been found to work more efficiently as the photoactive layer in Schottky-barrier OSCs using MoO_3-covered ITO substrates [18, 19]. Because the work function of MoO_3 can be as high as 6.8 eV, it is possible to form a huge electric field at the MoO_3/organic interface as a consequence of the electronic equilibrium there (see Sect. 10.4 for details). The resulting electric field may support carrier extraction and separation within the organic layer. Inserting an exciton blocking layer between the MoO_3 and the active layer can lead to a significantly improved
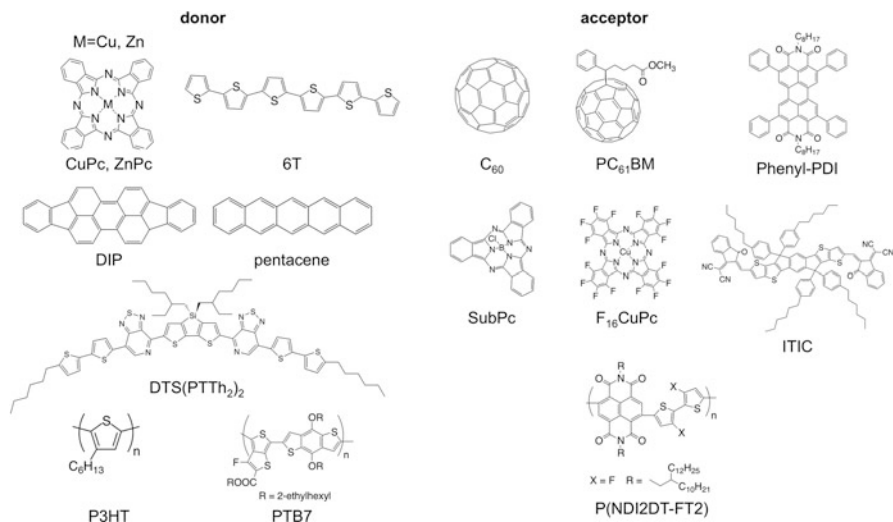
Fig. 10.3 Molecular structures of donors and acceptors used in OSCs. CuPc and ZnPc, copper and zinc phthalocyanine; 6T, sexithiophene; DIP, diindenoperylene; DTS(PTTh$_2$)$_2$, 5,5′-*bis*{(4-(7-hexylthiophen-2-yl)-[1,2,5]thiadiazolo[3,4-c]pyridine)-3,3′-di-2-ethylhexylsilylene-2,2′-bithiophene; P3HT, poly(3-hexylthiophene); PTB7, thieno[3,4-b]thiophene-*alt*-benzodithiophene copolymer; PC$_{61}$BM, [6,6]-phenyl-C$_{61}$-butyric acid methyl ester; SubPc, subphthalocyanine; F$_{16}$CuPc, perfluorinated CuPc; phenyl-PDI, *N,N*-bis(n-octyl)-2,5,8,11-tetraphenyl-PDI; P(NDI2DT-FT2), polymer composed of a 3,3′-difluoro-2,2′-bithiophene and a NDI with 2-decyltetradecyl side chains; ITIC, 3,9-bis(2-methylene-(3-(1,1-dicyanomethylene)-indanone))-5,5,11,11-tetrakis(4-hexylphenyl)-dithieno[2,3-d:2′,3′-d']-s-inddaceno[1,2-b,5,6-b']dithiophene

short-circuit current and fill factor and hence to a power-conversion efficiency of 2% [19]. Single-component OSCs comprising a donor-acceptor copolymer also show relatively high performance because photoelectric conversion occurs between the donor and acceptor components within a single molecule, thereby forming a clear carrier-transport path for charge extraction in the solid state [20, 21].

For more efficient carrier generation, a planar heterojunction (PHJ) of two dissimilar organic semiconductors (Fig. 10.4b) is preferable. This is because strongly bound excitons can split efficiently into free holes and electrons by using the energy offsets of the highest occupied molecular orbitals (HOMOs) or lowest unoccupied molecular orbitals (LUMOs) between the interfacing molecules as driving forces (see Fig. 10.5). Besides, transporting holes and electrons in the different materials supports that they can individually travel toward respective electrodes, which suppresses charge recombination. Molecules that transport holes and electrons are referred to as donors and acceptors, respectively. The molecules shown in Fig. 10.3 are classified roughly into these two categories.

A standard choice as the acceptor is C$_{60}$ because of its high electron affinity, excellent electron-transport ability, and low relaxation energy upon the formation of photo-generated anions. However, C$_{60}$ has relatively poor photoabsorption in the visible range, although that of C$_{70}$ is better because of a breakdown in molecular symmetry. There is also the difficulty of developing a synthesis
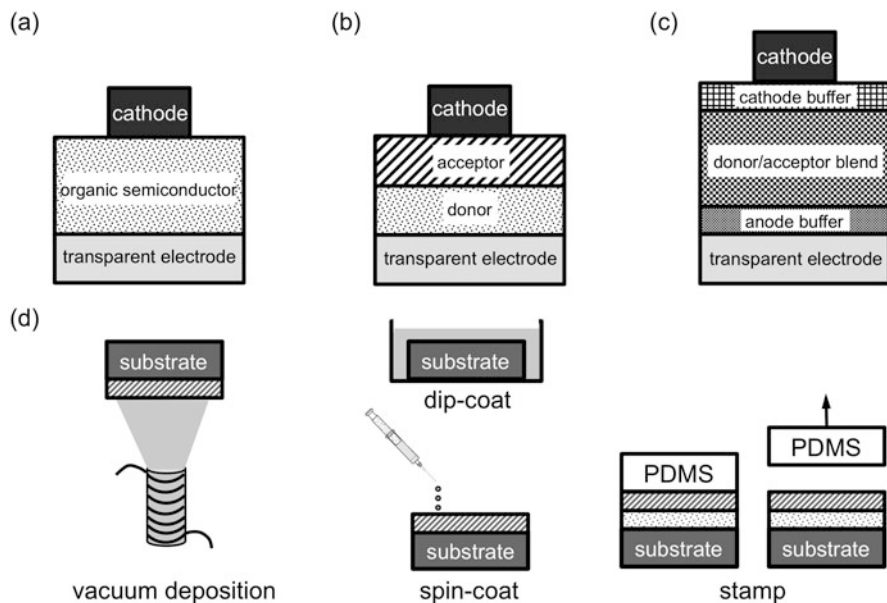
Fig. 10.4 Device structure (top) and corresponding energy diagrams (bottom) of an OSC. (**a**) Schottky-barrier OSC, (**b**) planar heterojunction (PHJ) OSC, (**c**) bulk heterojunction (BHJ) OSC. (**d**) Methods for preparing an OSC

method to modify the molecular structure in order to improve the photophysical and transport properties of such fullerene-based compounds, which escalates the associated costs. Instead, a series of small molecules based on perylene diimide, phthalocyanines, subphthalocyanines, truxenones, quinacridones, fluorenes, and *n*-type polymers with low energy gaps have been reported as promising acceptor molecules [22]. These have the advantages of low LUMO energy (which is achieved by introducing electron-withdrawing groups into its molecular structure), strong absorption in the visible region, adjustable frontier orbital energies by molecular design, morphological stability of the active layer in which they are used in, high thermal stability, and high solubility. For instance, the molecular architecture of the polymers enables them to have high solubility and a broad absorption spectrum. The many superior features of non-fullerene acceptor compounds and rapid developments in their method of synthesis mean that these compounds will play an important role in efficient OPVs in the near future [23, 24].

A disadvantage of a PHJ is that the donor/acceptor interface has a limited area. Hence, some of the formed excitons do not separate into free carriers and thus recombine before reaching the interface. To overcome this drawback, the concept of a bulk heterojunction (BHJ) has been proposed (Fig. 10.4c), wherein donor and acceptor molecules are blended [25, 26]. Because the BHJ interfacial area is much bigger than the PHJ one, tremendous opportunities are provided for exciton dissociation. The most efficient OSCs reported to date are based on this BHJ structure. Some BHJ-based OSCs with non-fullerene acceptors, combined
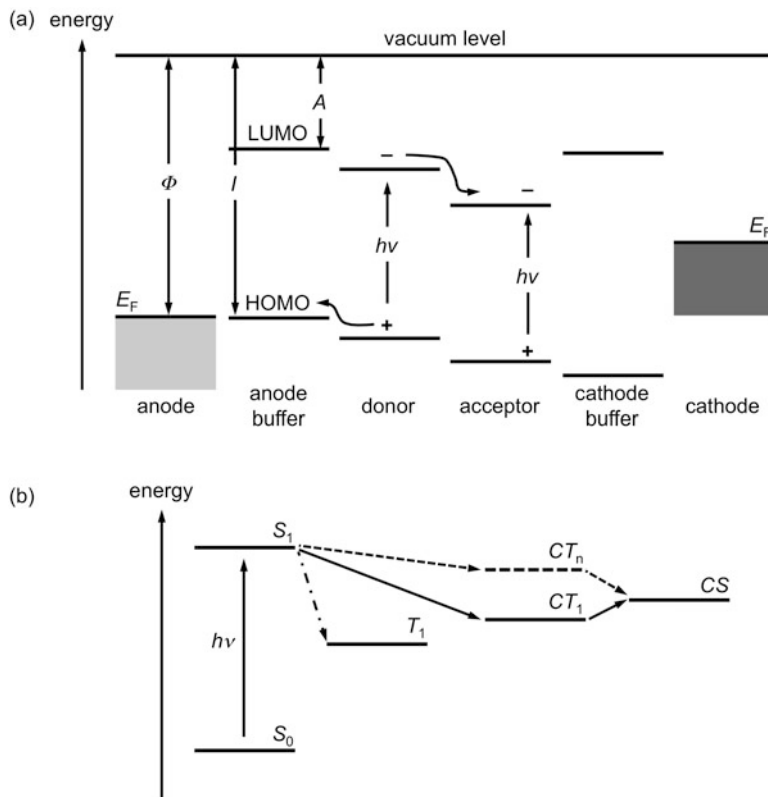
Fig. 10.5 (**a**) Schematic energy diagram of an OSC under the assumption of no built-in potential. Here the case for a planar heterojunction cell is shown. E_F is the Fermi level of the electrodes, hv denotes the photon energy of sunlight, Φ is the work function of the electrode, I is the ionization energy, and A is the electron affinity. (**b**) Corresponding electronic diagram: S_0 is the ground state; S_1 is the excited singlet state; T_1 is the excited triplet state; CT_1 and CT_n are the lowest and higher charge-transfer states, respectively; and CS is the charge-separation state

with state-of-the-art donor polymers, outperform their fullerene-based counterparts. For instance, the use of PTB7-Th as the donor and ITIC as the acceptor leads to efficiencies in excess of 11% [27], which demonstrates again that fullerenes and their derivatives are not the sole choice for OSC acceptors.

In these standard OSCs, holes (electrons) are extracted from the transparent electrode (Al and Ag cathode). However, the inverted geometry is also used (often called an inverted OSC), in which electrons are extracted from the bottom electrode while the top contact collects holes. In a standard OSC, acidic poly(3,4-ethylenedioxythiophene):poly(4-styrenesulfonate) (PEDOT:PSS) and calcium are the prototypical anode and cathode buffer layers, respectively. In spite of their versatility, these materials are sensitive to humidity and oxygen, and as such the long-term stability of OSCs employing these materials is poor. An inverted OSC can avoid the use of these materials because of (i) the commercially available of

relatively inert materials to lower the work function of the ITO bottom substrate (e.g., Cs_2CO_3 [28] and polyethyleneimine ethoxylated (PEIE) [29]) and (ii) the fact that the work function of the top electrode can also be controlled by, for example, evaporation of MoO_3.

The device architectures shown in Fig. 10.4a–c can be prepared using the methods illustrated in Fig. 10.4d. Vacuum deposition is the conventional way to prepare an organic thin film with high purity and crystallinity. The film thickness can be controlled precisely by using a quartz oscillator to monitor the amount and speed of deposition at the angstrom scale; these deposition features are estimated from changes in the intrinsic frequency of the quartz. A crucible containing the organic compound is heated resistively in a vacuum chamber, whereupon the sublimed molecules solidify on a substrate that is placed above the evaporation source. The substrate is ultrasonicated with solvents such as isopropanol, acetone, and pure water prior to the use, followed by UV-ozone treatment. Heating the substrate during the vacuum deposition increases the molecular mobility on the substrate surface, thereby improving the crystallinity of the formed film; this leads in turn to a thermodynamically stable molecular arrangement. However, vacuum deposition is of course applicable only to the sublimation of molecules with relatively low molecular weights.

Spin coating and dip coating offer alternative ways to form a thin film from compound solution on a desired substrate. A number of parameters can affect the morphology and crystallinity and consequently the charge transport and photophysical properties of the solution-processed film (e.g., the boiling point and evaporation rate of the organic solvent that is used, the film thickness, and the ratio of the mixed solvent). As for BHJ active layer, donor and acceptor components should preferably distribute in the normal direction for the selective charge transport (vertical phase separation), while attaining a large donor/acceptor interfacial area for efficient carrier generation. It is well known that P3HT molecules segregate upon being spin-coated on the surface of P3HT:$PC_{61}BM$-blend film because the P3HT surface energy is lower than the $PC_{61}BM$ one [30, 31]. Thermal annealing after deposition of the top electrode can suppress the surface segregation of P3HT [32].

Stamping is the other method for fabricating a multilayer OSC. A poly(dimethylsilane) (PDMS) stamp is used to transfer the active layer onto the substrate. With this stamping technique, one can fabricate multilayered BHJ and PHJ OSCs [33].

10.2 Operation Mechanism and Characterization of OSC

10.2.1 Photoabsorption

This process is the initial step in the operation of an OSC. If the photons have enough energy to excite electrons in the organic semiconductor from occupied states into unoccupied ones, light passing through a molecule will vibrate electrons bound to its positive nucleus by means of the time-dependent electric field of

the electromagnetic wave. As a result, the molecule gains (excitation) energy. For instance, electrons in the HOMOs of the donors and acceptors are excited into the respective LUMOs (Fig. 10.5a). As a result, an electrostatically bound hole-electron pair (exciton) is generated. To efficiently harvest the photons in the spectral irradiance distribution of sunlight, it is essential to engineer the band gaps of the organic semiconductor by introducing appropriate substituents and incorporating more than two semiconductors into the active layer. The absorption takes place on a femtosecond (10^{-15} s) timescale. The transition probability upon photoabsorption is proportional to the square of the transition moment $m = \int \psi_i\, e\mathbf{r}\, \psi_f\, d\tau$, where Ψ_i is the initial wave function [the ground state S_0 in Fig. 10.5b], Ψ_f is the final wave function [the excited state S_1 for a singlet exciton in Fig. 10.5b], and $e\mathbf{r}$ is the transition dipole operator. According to this relationship, the wave-function overlap between the initial and final states affects the magnitude of photoabsorption. The nature of photoabsorption of π-conjugated molecules is strong absorption in the visible range. Besides, the large geometrical relaxation upon excitation leads to broad absorption [34].

The direction of the transition dipole is determined by how the transition charge is distributed within the molecule. For most planar aromatic molecules, the transition dipole orients itself parallel to the atomic bond. Because the electric field of the incident light should match the direction of the transition dipole moment of the organic semiconductors, especially for elongated π-conjugated molecules, the likes of pentacene and phthalocyanine show the anisotropy of photoabsorption in the solid states. In this sense, it is critical to control the molecular orientation in order to produce a photocurrent. Specifically, for light absorption by π-conjugated molecules, the face-on and edge-on orientations (Fig. 10.6) are preferable to the end-on orientation (Fig. 10.6).

In addition to the absorption ability of each component in an OSC, we must take account of light interference within the OSC to understand the actual absorption within the device. This is because an OSC is made of multi-stacked organic and inorganic layers with different refractive indexes (Fig. 10.5a). The transfer-matrix method is widely used to model the light interference. In this method, the light traveling upstream and traveling downstream through the interfaces is added
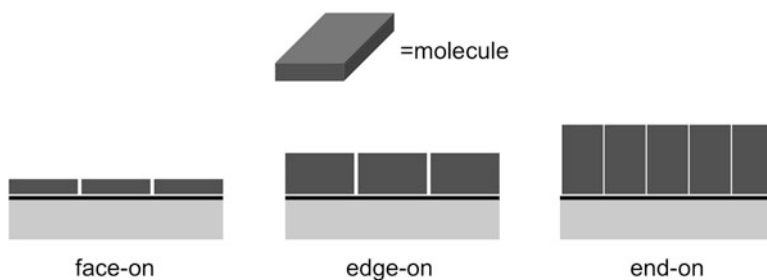

Fig. 10.6 Molecular orientations of a planar π-conjugated molecule

coherently to calculate the electric field strength of the standing waves in the stacks [34]. In this sense, metal reflectivity also plays a decisive role. For instance, calcium and samarium, which are at times used for the cathode electrode, show a relatively low photocurrent because of their weaker reflectance compared to the commonly used Al cathode [16].

10.2.2 Exciton Diffusion

The excitons that are generated upon photoexcitations have to diffuse to the donor/acceptor interface for free-charge separation. The state in which the spins in the occupied and unoccupied states are antiparallel is referred to as a singlet exciton. When the spins are parallel to each other, the state is referred to as a triplet exciton. This is generally spin-forbidden and thus does not form directly upon photoexcitation. However, in the case of strong spin-orbit coupling (e.g., in heavy-atom molecules such as sulfur or metals), transition from the singlet state to the triplet state is allowed. Exciton diffusion takes place through two energy-transfer mechanisms (Fig. 10.7):

(a) *Förster mechanism*

An electron that has been photoexcited into an unoccupied state moves more vigorously than it did when it was in the original occupied state because of the

Fig. 10.7 Förster and Dexter mechanisms for exciton transfer. Singlet excitons transfer via both schemes, whereas triplet excitons diffuse via only the Dexter mechanism. M_2 has a smaller band gap than M_1. M_1^* and M_2^* denote their excited states
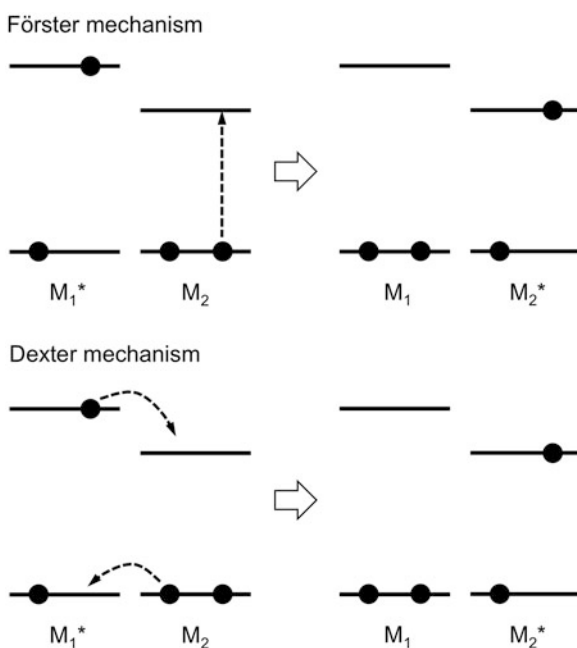
increase in the number of state nodes, and this results in the variance of the electric field within a molecule (call it M_1). If a neighboring molecule M_2 near the excited molecule $M_1{}^*$ can resonantly interact with the alternating electric field in M_1, M_2 will obtain excitation energy from M_1 and hence energy transfer occurs. In this mechanism, direct contact between M_1 and M_2 is unnecessary. Therefore, long-range (order of 10 nm) exciton diffusion is possible. As a rule of thumb, if the fluorescence spectrum of M_1 overlaps the absorption spectrum of M_2, an exciton can transfer via the Förster mechanism. Because this involves electronic transition from occupied to unoccupied states, only spin-allowed singlet excitons may diffuse using this mechanism.

(b) *Dexter mechanism*

In contrast to the Förster mechanism, the Dexter mechanism operates through direct molecular contact because it occurs via electron exchange through orbital overlaps. As a result, there is no spectral requirement and thus, in addition to singlet excitons, even triplet excitons can diffuse using this mechanism.

The exciton diffusion length L_D is given by $(D\tau)^{1/2}$, where D is the exciton diffusion constant and τ is the exciton lifetime. As mentioned previously, singlet excitons appear to have larger values of D than those of triplet excitons, but the latter have much longer lifetimes τ (on the order of microseconds) because relaxation of a triplet exciton to the ground state is spin-forbidden. In the solid state, the diffusion length as determined by, for example, photoluminescence quenching is 5–20 nm for both small molecules [35] and polymers [36], although an extremely long exciton diffusion length has been reported for single rubrene crystal (2–8 μm) [37]. In BHJ OSCs, excitons with short diffusion length L_D can reach the donor/acceptor interface efficiently because the domain sizes of donor and acceptor are comparable to L_D.

It is well known that metal can quench excitons at the interface to the photoactive layer. To prevent exciton quenching at the electrode interface, wide-band-gap molecules such as bathocuproine (BCP) and bathophenanthroline (Bphen) are inserted at the cathode interface (Fig. 10.5a).

10.2.3 *Free-Carrier Generation*

Excitons that reach the donor/acceptor interface may dissociate into free holes and electrons. Because of the relatively low dielectric constant (ε_r) of organic semiconductors ($\varepsilon_r = 3$–5), some driving force is necessary to generate free charges (typically several tenths of an electron volt). At the interface, photo-induced electron (hole) transfer occurs within 100 fs and is driven by the energy difference in the LUMO (HOMO) for excitons generated in donors (acceptors).

An important step on the way to free-charge separation is that, even after the photo-induced charge transfer, a hole in a donor and an electron in an acceptor are still bound to each other by Coulombic attraction before reaching the charge-separation (CS) state in which holes and electrons are completely free. This state

is referred to as the charge-transfer (CT) state. Although "hot" CT states [CT_n in Fig. 10.5b] have generally been regarded as the exclusive pathway to free charges [38, 39], Vandewal et al. showed that the internal quantum efficiency of many OSCs depends neither on whether band gap or CT states are excited nor on how energetic the CT states are [40]. These results suggest that "cold" CT states [the relaxed CT state CT_1 in Fig. 10.5b] could lead to the CS state. Apparently, CT_1 requires an activation energy to generate free charges. One possibility is that the binding energy of the CT states could be much lower than expected when we consider the change in the free energy of the system, namely, the entropy gain from charge dissociation [35, 41].

Some organic semiconductors such as acenes and diphenylisobenzofuran show singlet fission, in which a photoexcited high-energy exciton is converted into a pair of low-energy triplet excitons [T_1 in Fig. 10.5b] [42]. It is generally agreed that photoexcitation generates a triplet-pair state either coherently or incoherently from the singlet exciton and that this state may subsequently separate into two triplet excitons [42]. The underlying mechanism of singlet fission is now the subject of intense study.

10.2.4 Carrier Transport and Extraction

Once the charges are completely free, they drift and diffuse toward their respective electrodes with efficiencies that depend on their carrier mobilities. Because of the large electron-vibration coupling and the disordered nature of organic semiconductor layers, each charge is associated with a local geometrical relaxation and constitutes a polaron [34]. The molecular orientation of π-conjugated molecules is critical to enhancing carrier mobility. For small planar molecules, the face-on orientation is preferable for carrier transport. Recently, Ma et al. demonstrated that the end-on orientation of polythiophene further enhances hole mobility [43], although light absorption becomes weaker because of the orientational mismatch between the transition dipole moment of the polymer and the electric field of the incident light.

Carrier extraction at the electrode/organic interface is the final step in the operation of an OSC. The efficiency regarding this process is not determined simply by the frontier orbitals of the organic semiconductor and the Fermi levels of the electrodes. The electric field near the electrode interfaces, which is caused by the charge transfer in the ground states upon contact formation (see Sect. 10.4), also assists with carrier extraction. In addition, atomic diffusion of the metal electrode and the buffer materials may further complicate the interfacial phenomena. It is well recognized that to obtain long-term stability of an OSC, physical contact between the electrode and the active layer is critical, that is, matching the surface energies of the contacting materials. However, deep and comprehensive understanding of this process still appears to be lacking.

10.2.5   Characterization of OSC

A solar cell is characterized by measurements of its current density (J)-voltage (V) curve under AM1.5 illumination. Its power-conversion efficiency (η) is given by

$$\eta = \frac{J_{max} V_{max}}{P_{in}} = \frac{J_{sc} V_{oc} FF}{P_{in}}, \tag{10.1}$$

where P_{in} is the power of the incident light, J_{max} and V_{max} are the maximum current density and voltage, respectively, J_{sc} is the short-circuit current, V_{oc} is the open-circuit voltage, and FF is the fill factor (Fig. 10.8a). Here, FF can be regarded as the ratio of $J_{max} V_{max}$ to $J_{sc} V_{oc}$. According to Eq. (10.1), it is necessary to optimize J_{sc}, V_{oc}, and FF to improve the overall power-conversion efficiency. The equivalent circuit for the solar cell is illustrated in Fig. 10.8b. It consists of a diode with a reverse-saturation-current density (J_0) and ideality factor (n), a current source corresponding to the photocurrent (J_{ph}), a series resistance (R_s) resulting from the contact resistance between the semiconducting material and the electrode and from the conductivity of the building components of the OSC, and a shunt resistance (R_p) derived from the loss of carrier recombination centers. The measured J-V curves are often analyzed using the generalized Shockley equation

$$J = \frac{1}{1 + R_s/R_p} \left[J_0 \left\{ \exp\left(\frac{V - JR_s A}{nkT/e} \right) - 1 \right\} - \left(J_{ph} - \frac{V}{R_p A} \right) \right], \tag{10.2}$$

where e denotes the elementary charge, kT is the thermal energy, and A is the area of the cell. From the above equation, J_{sc} can be expressed as
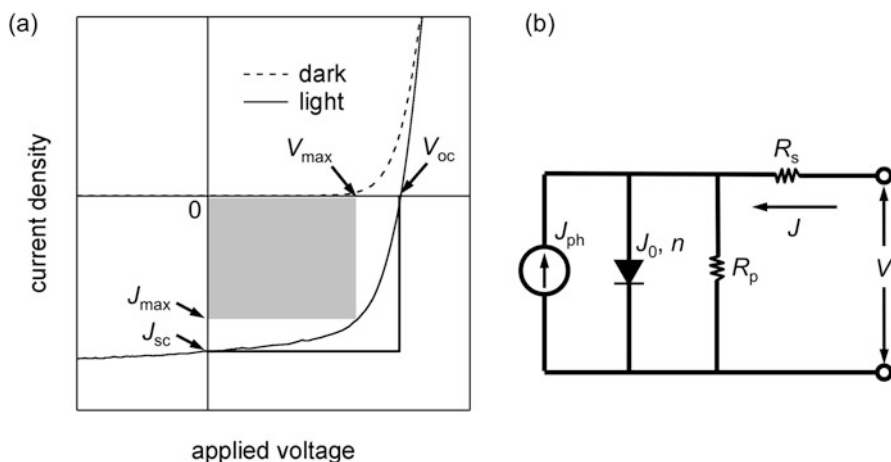

Fig. 10.8 (a) Current-density-voltage characteristics of solar cell in dark and illuminated conditions. (b) Equivalent circuit for solar cell. The notation is defined in the text

$$J_{sc} = -\frac{1}{1 + R_s/R_p} \left\{ J_{\mathrm{ph}} - J_0 \left(\exp\left(\frac{|J_{\mathrm{sc}}| \, R_s A}{nkT/e} \right) - 1 \right) \right\}. \tag{10.3}$$

By fitting the measured J-V curve with Eq. (10.2), we can obtain values for the parameters R_s, R_p, and n.

10.2.5.1   Short-Circuit Current Density (J_{sc})

The maximum photocurrent J_{sc} is calculated by

$$J_{\mathrm{sc}} = \int_{\mathrm{AM1.5}} e\eta_{\mathrm{EQE}}(\lambda) \, N_{\mathrm{ph}}(\lambda) \, d\lambda, \tag{10.4}$$

where $N_{\mathrm{ph}}(\lambda)$ is the photon flux density in the incident AM1.5 G spectrum at wavelength λ and $\eta_{\mathrm{EQE}}(\lambda)$ is the external quantum efficiency that indicates the fraction of photons that are converted into current at wavelength λ. The upper limit of J_{sc} is calculated by integrating Eq. (10.4) from the high photon energy side to the wavelength corresponding to the optical band gap of the material. For example, silicon's band gap is 1.1 eV, yielding $J_{\mathrm{sc}} = 43.6$ mA cm^{-2}. To enhance J_{sc}, the optical band gaps of the organic donor and acceptor should be low enough and cover sufficiently different optical ranges of sunlight.

According to Eq. (10.3), large R_s (contact resistance and bulk resistance) is detrimental to obtaining high J_{sc}. Therefore, the more conductive is the semiconducting material, the more current density is available. Charge density and mobility within the organic layer also impact J_{sc}.

10.2.5.2   Open-Circuit Voltage (V_{oc})

The physical origin of V_{oc} for an OSC has been discussed rigorously, and it has been found that its value is influenced by the work function of the electrode material, the donor ionization energy, and the acceptor-electron affinity [44–47]. According to conventional semiconductor physics, the maximum value of V_{oc} is the difference between the quasi-Fermi levels of the semiconductor holes and electrons (E_{Fp} and E_{Fn}): [48]

$$qV_{\mathrm{oc, \, max}} = \left(E_{\mathrm{Fn}} - E_{\mathrm{Fp}} \right)_{\mathrm{max}}. \tag{10.5}$$

That is, the band gap of the semiconductor determines the maximum value of V_{oc} for an inorganic solar cell. If we simply apply the same principle to an OSC, the maximum V_{oc} can be determined by the energy difference between the donor HOMO and the acceptor LUMO (i.e., the photovoltaic gap). Actually, this relationship was confirmed by comparing the photovoltaic gaps determined by photoelectron spectroscopy and by measured V_{oc} (Fig. 10.9) [49, 50].

Fig. 10.9 Correlation between measured V_{oc} and ionization energy of donor and electron affinity of acceptor. (Reprinted with permission from Ref. [49]. Copyright 2017 American Chemical Society)
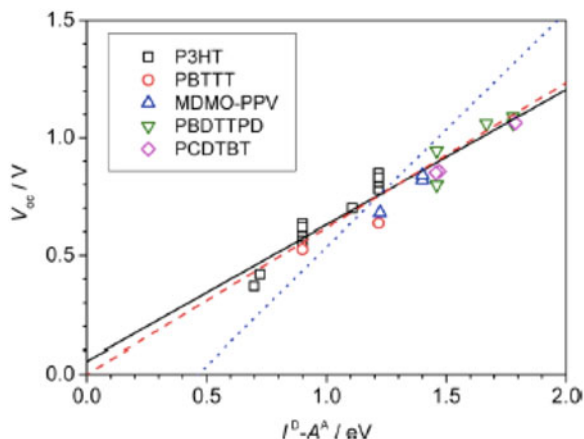
However, there is an empirical relationship that V_{oc} is 0.5–0.7 V smaller than the photovoltaic gap, which is confirmed experimentally by comparing V_{oc} and the gap measured with photoelectron spectroscopy [50]. To understand the origins of V_{oc} and its loss comprehensively, it has been proposed that V_{oc} be determined by the energy of the CT state (E_{ct}) [51]:

$$E_{ct} = E_0 - E_B, \tag{10.6}$$

where E_0 denotes the difference in energy between donor-ionization energy and acceptor-electron affinity (the energy difference between peaks of Gaussian donor-HOMO and acceptor-LUMO) and E_B is the average binding energy of the CT state:

$$E_B = \frac{q^2}{4\pi \varepsilon r_{ct}}, \tag{10.7}$$

where ε denotes the dielectric constant of the material and r_{ct} is the average separation between holes and electrons in the CT state. Burke et al. recently established a model in which CT states and free carriers are in equilibrium [52] and derived the following relationship for V_{oc}:

$$q V_{oc} = E_{ct} - \frac{\sigma_{ct}^2}{2kT} - kT \log\left(\frac{qf N_0 L}{\tau_{ct} J_{sc}}\right), \tag{10.8}$$

where σ_{ct} denotes the dispersion of the CT state (Gaussian in shape), k is the Boltzmann constant, T is temperature, f is the volume fraction of the mixed region in the active layer, N_0 is the density of states in the organic material, and τ_{ct} is the lifetime of the CT state. From Eq. (10.7), one can easily see that the value of V_{oc} is influenced by not only E_{ct} but also the degree of disorder of the CT state, the interfacial area between donor and acceptor, and how recombination at the

donor/acceptor interface is suppressed. Besides, Eq. (10.7) indicates that increasing the distance between holes and electrons in the CT state weaken the Coulomb interaction between the states, presumably resulting in an improved V_{oc}.

10.2.5.3 Fill Factor (FF)

As mentioned before, *FF* is the ratio of the obtainable maximum power to the product of J_{sc} and V_{oc}. For an OSC with a high *FF*, the photocurrent should remain unchanged when forward bias is applied. In turn, photo-generated carriers drift efficiently through the active layer and electrode interfaces. In other words, series resistance R_s should be low enough for achieving high *FF*. Therefore, the organic and inorganic materials used in an OSC must be "neat" in relation to both purity and molecular order in the film without a carrier-extraction barrier at the electrode interfaces through which free charges pass. In general, relatively high mobility and appropriate control of molecular orientation are required. Impurities in organic semiconductors may act as charge traps [15, 16] and thus must be removed by train sublimation and solvent purification, for instance. Besides, the hole/electron mobility balance affects the fill factor because such an imbalance leads to carrier accumulation near the donor/acceptor interface, which leads to an *S*-shaped *J*-*V* curve and lowers *FF* [53].

Ohmic contact at the electrode interfaces, where contact resistance is negligible for both carrier injection and extraction, is also required for enhancing *FF*. The ideal contact can be achieved by modifying the electrode surface appropriately to obtain the desired work function, thereby achieving Fermi-level pinning (see Sect. 10.4). For example, the value of R_s of a DIP/C_{60} PHJ OSC prepared on unannealed PEDOT:PSS is 42 kΩ, whereas thermal annealing of PEDOT:PSS increases its work function and concurrently leads to a significantly reduced R_s (down to 55 Ω). Consequently, the *FF* of the OSC increases to 0.74 [54].

10.3 Electronic Properties of π-Conjugated Molecules

The electronic structure of donor and acceptor molecules is known to have a great influence on the device performance of OSCs, particularly the optical absorption, carrier injection, and carrier transport because they have a good deal to do with the operation principle of the devices. As mentioned in Sect. 10.2.5.2, V_{oc} is proportional to the energy difference between the donor's HOMO and the acceptor's LUMO. Therefore, whether intentionally or not, manipulating the molecular structure of donors or acceptors sometimes changes their electronic structure and can affect the device performance. Determining the correlation between the electronic structure of the materials and the function of the OSCs would guide the future material design.

It has been reported that the C_{60} fullerene is a good acceptor for OPVs because of its high electron transfer rate from donor molecules. However, because of the necessity to use soluble compounds when making a device with a BHJ structure, fullerene derivatives such as $PC_{61}BM$ (Fig. 10.3) were developed. The C_{60}- and C_{70}-based PCBMs have been used frequently as acceptor molecules in OPVs, together with π-conjugated polymers such as P3HT as the donor. By using BHJs that combine PCBMs (thereby maintaining a high electron transfer rate) and π-conjugated polymers (thereby ensuring high carrier mobility), we guarantee devices with high power-conversion efficiency. The point of interest here is that by tuning the molecular structure of the fullerenes to achieve soluble derivatives, we end up unintentionally modifying the electronic structure. In some cases, this change in electronic structure can be measured in the device performance.

10.3.1 Fullerene Derivatives

The high symmetry of the molecular structure of fullerenes C_{60} and C_{70} yields a low back electron transfer rate after charge separation occurs. It is also responsible for a highly efficient intersystem crossing from singlet to triplet excited states, giving excited states with long lifetimes. These characteristics make these compounds indispensable as acceptors for OSCs. Fullerenes C_{60} and C_{70} are incompatible with the solution processes such as spin coating because of their low solubility in common organic solvents. Soluble derivatives have been synthesized by adding functional groups to these fullerene backbones [55, 56], thereby allowing OSC devices to be produced using solution processes such as spin coating [57]. Now, C_{60} and C_{70} derivatives bearing various functional groups, which improve solubility and processability, have been used as acceptors in BHJ-OSC with high-efficiency photoelectric conversion [58–62]. PCBMs based on C_{60} and C_{70} are well-known soluble derivatives and have been used frequently as an acceptor in OSCs [55, 58]. It has been reported that the side chains of $PC_{61}BM$ affect the film morphology, which may improve the device performance [63–66].

Akaike et al. [62, 66] reported that adding a side chain to a C_{60} backbone affects not only its solubility but also the electronic structures of $PC_{61}BM$ and [6,6]-diphenyl-C_{62}-bis(butyric acid methyl ester) (bis$PC_{61}BM$). They concluded that a subtle charge transfer from the side chain to the C_{60} backbone destabilizes the frontier orbitals of the molecule. They also suggested that the effects of the side chain on the electronic structures of $PC_{61}BM$ and bis$PC_{61}BM$ may improve the performance of the OSC devices compared with devices containing C_{60} [67, 68]. Their work demonstrates that measures of OSC device performance such as V_{oc} can be discussed in terms of electronic structure.

The results of ultraviolet photoemission spectroscopy (UPS) and inverse photoemission spectroscopy (IPES) for $PC_{61}BM$, bis$PC_{61}BM$, C_{70}, and $PC_{71}BM$ are shown in Fig. 10.10. The simulated spectra based on the molecular orbital calculation are also displayed (filled in gray). The combined UPS and IPES spectra
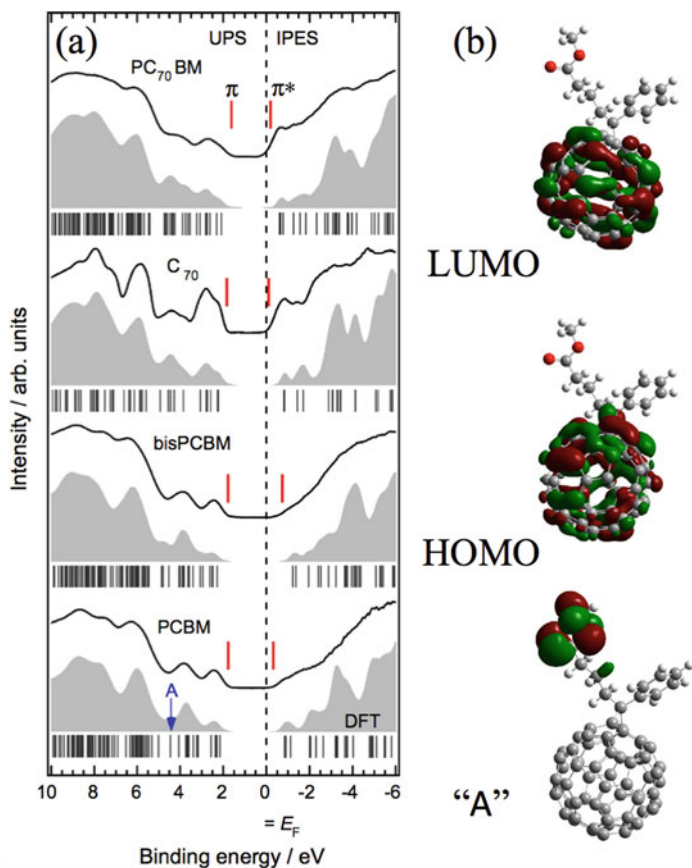
Fig. 10.10 (**a**) Ultraviolet photoemission spectroscopy (UPS) and (**b**) inverse photoemission spectroscopy (IPES) spectra for fullerene derivatives. (Reprinted with permission from Ref. [65])

replicate the molecular orbitals (MOs) of the specimen. Indeed, the simulated spectra reproduce the observed spectra well. The HOMO, LUMO, and highest occupied MOs in the side chain labeled "A" are displayed in Fig. 10.10b. The MOs in the side chain are located at binding energies in excess of 4 eV. Basically, the π-orbitals of the C_{60} backbone contribute greatly to the HOMO and LUMO of the derivatives as seen in the case of $PC_{61}BM$ in Fig. 10.10a, b. The vertical bars in Fig. 10.10a indicate the onsets of the UPS and IPES spectra that correspond to the HOMO (π) and LUMO (π^*) energies. The energy difference of the HOMO measured from E_F is the height of the hole injection barrier ϕ_h^{exp}, and the energy difference between the LUMO and Fermi level (E_F) is the height of the electron injection barrier ϕ_e^{exp} from the electrode. The adiabatic ionization energy I^{exp}, electron affinity A^{exp}, and energy gap E_g^{exp} can be calculated from ϕ_h^{exp}, ϕ_e^{exp}, and E_{vac}. Here, E_{vac} denotes the vacuum-level energy obtained directly by the UPS
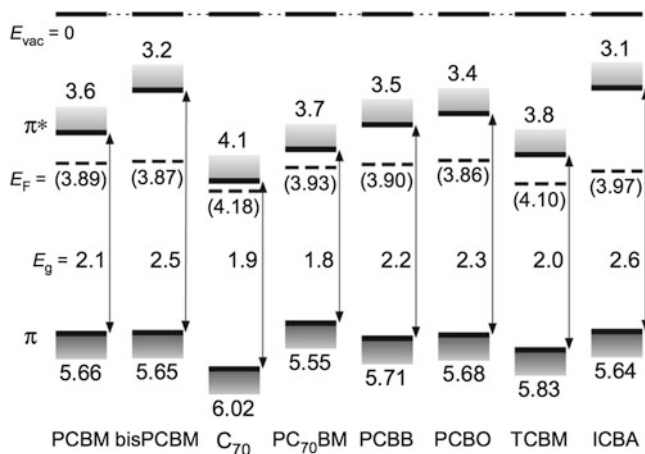
Fig. 10.11 Energy diagrams for various fullerene derivatives determined by UPS and IPES

experiments. The values of ϕ_h^{exp}, ϕ_e^{exp}, and E_g^{exp} calculated from the UPS-IPES spectra for the compounds in Fig. 10.10a are summarized in Fig. 10.11. The LUMOs of all the compounds are very close to E_F, and the low-lying LUMO explains the n-type electric characteristics of the devices in which they are used. The LUMOs of C_{70} and $PC_{71}BM$ are right above E_F, indicating very small ϕ_e^{exp}. In contrast, the LUMOs of bisPCBM and ICBA are higher than the LUMOs of the other fullerene derivatives, which probably causes the larger V_{oc} of the OPV devices containing bisPCBM or ICBA.

The values of I_{exp}, A_{exp}, and E_g^{exp} differ among all the fullerene derivatives. There is more variation in the LUMO energies than in the HOMO ones. The I_{exp} and A_{exp} values of C_{70} are larger, and the A_{exp} values of bisPCBM and ICBA are smaller than those of the other compounds. The E_g^{exp} values of C_{70} and $PC_{71}BM$ are smaller, and the E_g^{exp} values of bisPCBM and ICBA are larger than those of the other compounds. The small E_g^{exp} value of $PC_{71}BM$ causes a wide absorption range in the visible region, which leads to the high power-conversion efficiency of the OSC devices in which $PC_{71}BM$ is used as an acceptor [59–61].

Akaike et al. [62, 66] explained the effects of the side chain on the electronic structure of $PC_{61}BM$ and $bisPC_{61}BM$ by slight polarization of the electron density inside the molecules. A subtle electron transfer from the side chain to the C_{60} backbone destabilizes the frontier orbitals spreading over the fullerene backbone. The side chain donates a certain amount of electron density to the C_{60} backbone. The amounts of charge in $PC_{61}BM$ and $bis-PC_{61}BM$ donated to the backbone are estimated at roughly $0.23e$ and $0.46e$, respectively, from the density functional theory (DFT) calculations, where e is the elementary charge. Thus, the partial electrical charge donated from the side chain to the C_{60} backbone of $PC_{61}BM$ and bisPCBM destabilizes the HOMO and LUMO of the molecule and lowers both the I_{exp} and A_{exp} values. This indicates that PCBM and bisPCBM are weaker acceptors than C_{60}.

10.3.2 π-Conjugated Donor Polymers

Semiconducting π-conjugated polymers such as polyphenylenes, polyphenylenes, polyanilines, and polypyrroles have been used frequently in organic electronic devices including OPVs because they possess high solubility in organic solvents and can be formed into smooth films by solution processes. A series of conjugated polymers, poly(3-alkylthiophene)s (P3ATs), is widely used as a hole-transporting material in organic field-effect transistors (OFETs) and OSCs [57, 69–73]. The mobilities of the OFETs with P3HT reach 0.1 cm^2 V^{-1} s^{-1} [69–73], which is comparable to that of amorphous silicon-based FETs. This dramatic improvement in hole mobility has been attributed to the high degree of intra-chain and interchain orders in the P3AT films. The structure of P3HT films as deduced by X-ray diffraction (XRD) analysis is composed of polycrystalline domains embedded in an amorphous matrix [74, 75]. In the polycrystalline domain, P3HT stacks in one-dimensional chains and forms a lamellar structure consisting of two-dimensional conjugated sheets through interchain stacking. The degree of structural order in P3AT films depends strongly on the degree of regioregularity of the polythiophene backbone [76]. It is thought that the conformation and packing of the polymer backbone play a dominant role in determining the transport properties of the material. As mentioned above, OFETs with highly regioregular P3HT have high mobility, whereas OFETs with regiorandom P3HT have mobilities in the range of only 10^{-5}–10^{-4} cm^2 V^{-1} s^{-1} [77]. The high mobility of regioregular P3HT films is partly attributable to the highly ordered structure of the film.

The morphology of the regioregular P3HT polycrystalline film or domains in the active layer in OSCs changes considerably upon annealing, as shown in Fig. 10.12a. Figure 10.12b displays a schematic of the microcrystalline structure
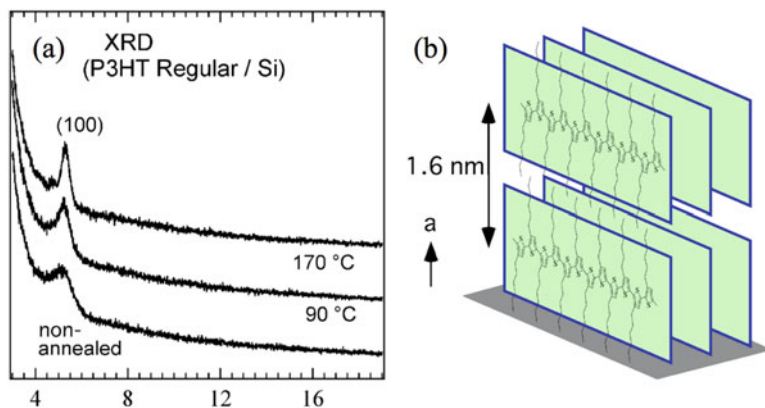

Fig. 10.12 (**a**) XRD of P3HT film prepared under different conditions coated on silicon substrates. (**b**) Schematic illustration of molecular arrangement of P3HT. (Reprinted with permission from Ref. [79])

of P3HT. In the polycrystalline domain, P3HT stacks in one-dimensional chains and forms a lamellar structure consisting of two-dimensional conjugated sheets through interchain stacking. The structural order in P3AT film depends strongly on the degree of regioregularity of the polythiophene backbone [76]. The electrical properties of P3HT films are also affected by annealing: the mobility is dramatically improved [78]. The increased mobility due to annealing is accompanied by increased structural order as observed by atomic force microscopy and X-ray analysis [79]. This result is in contrast to the interpretation that grain boundaries are the major cause of low mobility in low-molecular-weight P3HT films since the annealed films have high crystallinity [79]. Zen et al. have suggested that the main cause of the low mobility of the low-molecular-weight P3HT films is the disordered conformation of the backbones of a majority of the polymer chains, which hinders interchain charge transport as a result of fewer interchain contacts [77]. Alternatively, polymer chains of higher-molecular-weight P3HT possibly have more extensive π-conjugation, which would provide more opportunities for charge carriers passing along the polymer chain to hop to a neighboring polymer through an interchain contact.

Also, we have measurable effects induced by annealing in the electronic structure of the P3HT films. It was found that annealing strongly influences the energy gap, the energy of vacuum level, and the π- and π*-band energies. Consequently, the carrier injection barriers at the interfaces between the P3HT film and the electrodes are significantly affected. Figure 10.13 shows the combined UPS and IPES spectra of the regioregular P3HT films on ITO substrates. The π-band onset in the non-annealed sample is very close to E_F and shifts to higher binding energies after annealing, whereas the vacuum level and the π*-band onset are less affected. The high-resolution IPES spectra of the annealed films are more structured with the appearance of shoulders, denoted in the figure by arrows. In addition, the UPS spectra at the onset of the π-band become more structured after annealing. Simulated spectra derived from the calculations based on DFT are shown in Fig. 10.13. The simulations were performed using a hexylthiophene oligomer with 10 repeating units of 3-hexylthiophene rings ($n = 10$; 10HT) as a model system. Ten repeating units of HT are enough to reproduce the polymer qualitatively; therefore, 10HT is a good model system for discussing the electronic structure of P3HT. The simulated spectra reproduce the measured spectra well. Based on a comparison of the observed and simulated spectra, the shoulder structures at ∼3.5 eV above E_F (indicated by arrows) are assigned to the π*-band. The energy of the band is almost independent of the number of repeating units, and the HOMO and LUMO of 10HT are composed primarily of the π- and π*-orbitals distributed over the conjugated polymer chain. It is clear that the π- and π*-bands grow after annealing as the π-conjugation length increases by a conformation change of the polymer chain. These results are consistent with the change in the UV-visible spectra after annealing [79].
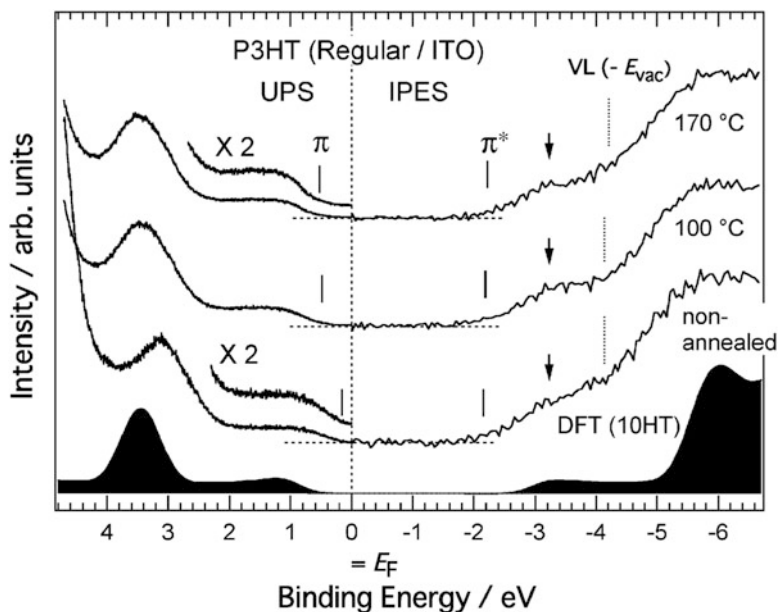
Fig. 10.13 UPS and IPES spectra of rr-P3HT thin films spin-coated on ITO substrate. (Reprinted with permission from Ref. [79])

10.4 Electrode/Organic Interface and Organic Heterointerface

The interface between the electrode and organic semiconductor in an active layer should be free from any energetic barrier to carrier extraction. Thus, we have to realize ohmic contact (i.e., negligible contact resistance with respect to the total resistance) of an OSC. A question arises as to what constitutes ohmic contact for an electrode/organic interface. In the case of an inorganic semiconductor, it is known that high doping concentration and a low energy barrier reduce the contact resistance [48]. Although organic semiconductors are typically *undoped*, the molecules at the interface to the electrode can be *doped* as a result of electron transfer to achieve thermodynamic equilibrium upon contact formation. Such a contact-induced doping has been demonstrated for a high-work function substrate/donor polymer interface and low-work function substrate/C_{60} interfaces [80–83]. Besides, the charge density distribution leads to evolution of an electrostatic potential near the electrode interface, thereby impacting the relative energy of the frontier orbitals with respect to the electrode Fermi level (E_F). Because the energetic landscape near the interface can significantly affect carrier processes and hence OSC performance, knowledge of the mechanism for charge-density and potential distribution is essential for designing the interface.

In this section, we introduce a recently proposed model that simulates energy-level alignment at the interface, which is applicable to electrode/organic interfaces as well as to organic heterointerfaces. Next, we discuss the technique that control electrode work function and wettability to improve energy matching and physical contact between the organic semiconductor and the electrode surface, along with correlating the interface property with the OSC performance.

10.4.1   Theoretical Model for Energy-Level Alignment

Recently, Oehzelt et al. proposed a comprehensive electrostatic model of the energy-level alignment, which is applicable even to organic heterointerfaces [84]. The model assumes that (1) the conductive substrate is an electron-reservoir, (2) the electron occupation obeys Fermi-Dirac statistics under thermodynamic equilibrium and electrons move through the organic layer toward the electrode E_F or vice versa, and (3) organic layers are grown ideally in a layer-by-layer manner on a conductive substrate with experimentally determined HOMO and LUMO onsets, density of states width, and a discrete height z. The charge density at each layer is calculated by

$$\rho(z) = e \cdot n \cdot \left\{ \int_{-\infty}^{+\infty} f_H(E) \cdot D_H\left[E + eV(z)\right]\, dE - \int_{-\infty}^{+\infty} f_L(E) \cdot D_L\left[E + eV(z)\right]\, dE \right\}, \tag{10.9}$$

where e is the elementary charge; n is the molecular number density per area layer; f_H and f_L are Fermi-Dirac functions; D_H and D_L are the peak shapes for the HOMO and LUMO, respectively (typically Gaussian); and $V(z)$ is the potential at distance z from the substrate surface. The charge density so obtained is used to calculate the potential in the respective layer using a generalized one-dimensional Poisson equation:

$$\nabla\left(\varepsilon_r(z)\nabla V(z)\right) = -\frac{\rho(z)}{\varepsilon_0}, \tag{10.10}$$

where $\varepsilon_r(z)$ is the dielectric constant of the layer and ε_0 in the permittivity in a vacuum. The obtained potential is used to calculate charges by solving Eq. (10.9) again, and then a new $V(z)$ is calculated. This self-consistent calculation can simulate depth-resolved charge density and potential distributions. The simulation results can reproduce the trend of thickness-dependent UPS measurements, which are traditionally used to determine the potential distribution along the surface normal. Combining the model simulation and UPS analysis, Wang et al. revealed that the upward band bending at the Ag(111)/NaCl/C_{60} heterostructure, which is attributed to electron transfer from Ag to C_{60} through the NaCl layers, is caused by the evolution of electron density in the C_{60} layers up to 150 nm [80].
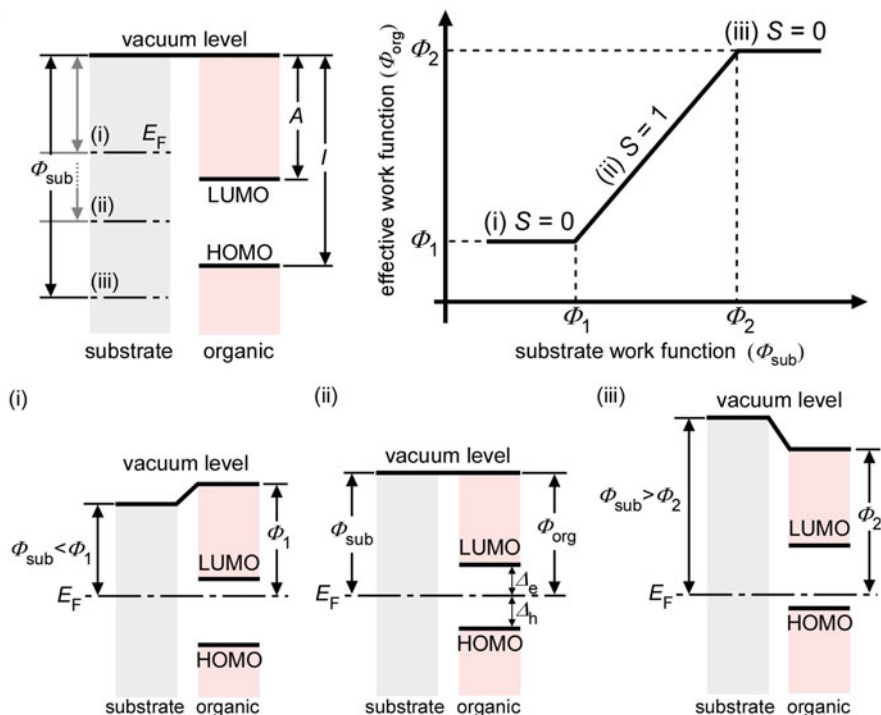
Fig. 10.14 Energy-level alignment at organic interface. Φ_{sub} denotes substrate work function, A is the electron affinity, and I is the ionization of the organic molecules. When Φ_{sub} exceeds I (A), the effective work function of the organic layer (Φ_{org}) is independent of Φ_{sub} [regions (i) and (iii)]; otherwise, Φ_{org} depends on Φ_{sub} [region (ii)]. In the regions (i) and (iii), Fermi-level pinning occurs. S denotes the slope parameter that is defined as $d\Phi_{org}/d\Phi_{sub}$

The model also predicts the dependence of energy-level alignment at the interface on the substrate work function. As already demonstrated by UPS measurements [85, 86], when the substrate work function is higher (lower) than the ionization energy (electron affinity) of the molecule, the vacuum and energy levels are independent of the substrate work function (Fig. 10.14). This phenomenon is known as "Fermi-level pinning," [85] being reminiscent of the constant charge-injection barrier occurring at a metal/inorganic semiconductor junction because of the dangling bonds.

Typically, the electronic structure at metal/organic interfaces is investigated for organic molecules adsorbed on a metal surface. However, if an interface between the photoactive layer and the top cathode is formed by vacuum deposition, the morphology and electronic structure at the interface can be different from those of the interface with the reversed deposition sequence. For instance, whereas an Au(111)/NPD interface seems to be inert and there is no strong interaction between the two constituents, gold atoms vacuum-deposited on NPD lead to a new chemical species as revealed by XPS [87]. The asymmetry of the electronic structure actually

leads to different charge-injection barriers in diode devices. Usually, injecting from the top contact is more efficient than doing so from the bottom contact [88].

10.4.2   Modification of Electrode/Organic Interfaces

As mentioned above, controlling the work function and morphology is critical to achieving ohmic contact for a more efficient device. So far, various materials including transition metal oxides, alkali halides, a polymer electrolyte, an inorganic salt, and a self-assembled monolayer (SAM) have been employed as interface modifiers for an OSC [89, 90]. In addition, here we introduce interface organic materials that are often used for OSCs to control their electronic, morphological, and photophysical properties.

10.4.2.1   Control of Electrode Work Function

To realize an ohmic contact, the Fermi levels of the anode and cathode should be close to the HOMO of the donor and the LUMO of the acceptor, respectively. Actually, Fermi-level pinning is important for reducing the series resistance of an OSC, leading to improved J_{sc} and FF [16]. Therefore, appropriate control of the work function of the anode and cathode is required. It was found for ITO substrates that the surface treatments such as UV/ozone, oxygen plasma, and dipping in aqueous alkaline hydroxide solution alter the surface chemical composition and work function because of the formation of surface dipoles and the removal of carbon contamination from the substrate surface. Among anode interface materials, PEDOT:PSS (whose molecular structure is shown in Fig. 10.15) has been used as a polymer-based anode interface layer to improve hole extraction. Its work function ranges from 4.5 to 5.6 eV, depending on its composition and heat treatment [91, 92], which can pin the HOMO levels of most donors to the Fermi level of the substrate. Figure 10.16 shows the importance of the Fermi-level pinning of the donor HOMO in optimizing the OSC behavior. Wagner et al. demonstrated that Fermi-level pinning is necessary to avoid an undesirable S-shaped I-V curve due to a high series resistance that can lower the FF of the OSC [16, 54].

Despite its wide-ranging applicability, the long-term stability of OSCs prepared on PEDOT:PSS is poor because of traps that form through water diffusion and because of the increased contact resistance due to water damage to the cathode [93]. Instead of the polymer buffer layer, transition metal oxides such as MoO_3 and V_2O_5, and phosphonic SAM, have been employed to control the anode work function. The oxides have very high work functions up to 7 eV, independent of the bottom substrate work function because of its n-type character that results from a finite concentration of oxygen defects even in pristine MoO_3 evaporated films [94]. This high work function leads to a downward energy shift in the photoactive layer because of the hole accumulation therein, probably leading to exciton dissociation
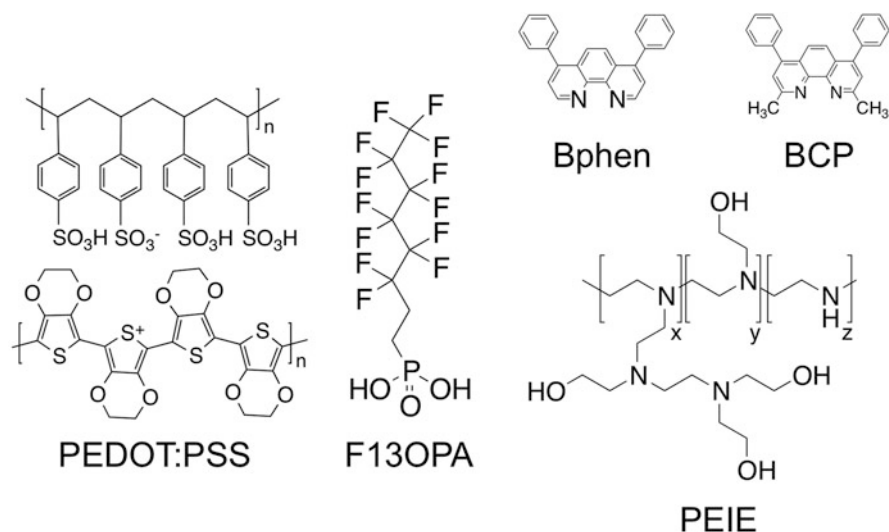
Fig. 10.15 Molecular structure of representative interface modifier

and efficient hole extraction. Actually, the Schottky-barrier OSC based on C_{60} and SubPc shows relatively high performance [18, 19].

The substrate work function actually affects not only the interface energetics but also the photophysical behavior of an OSC. Knesting et al. investigated the correlation between work function modification with V_{oc} and carrier lifetimes [95]. A higher work function leads to a higher electric field at the anode/photoactive-layer interface, suppressing carrier recombination in the bulk. Wang et al. recently reported that the contact-induced doping, which is due to the Fermi-level pinning, may decrease the photocurrent. Thus, there is an optimal work function for the respective polymer to keep its built-in field [96], in contrast to other reports that there is no dependence of OSC performance on substrate work function [97, 98]. A detailed study of carrier distribution (in the ground states) and carrier generation/recombination processes is necessary to obtain a comprehensive understanding of the impact of interface energetics on the device characteristics.

In standard OSCs, lithium fluoride (LiF), bathocuproine (BCP), and bathophenanthroline (Bphen) have often been used as cathode modifiers. By inserting thin films of these materials at the interface between C_{60} and Al, the overall performance of PHJ OSCs improves significantly because of suppression of nonradiative recombination of excitons at the C_{60}/Al interface [99], thereby increasing the interfacial electric field [100]. Toyoshima et al., employing UPS, reported a large work function reduction upon depositing BCP onto metallic substrates [101, 102]. Despite the findings that the large downward energy shift at the C_{60}/BCP interface leads to efficient electron extraction [103, 104] and BCP-thickness-dependent energy-level alignment at the Ag/BCP/C_{60} heterostructure
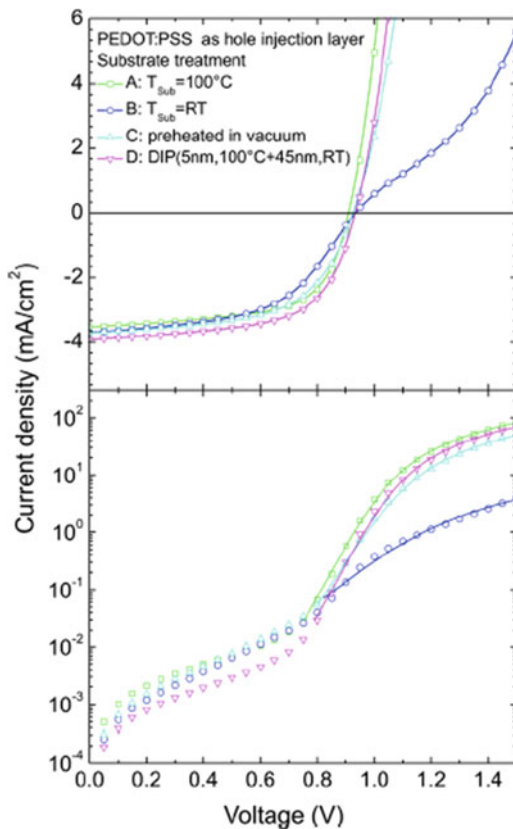
[105], direct correlation between the interfacial electronic structure and OSC performance remains elusive.

For an inverted OSC, the work function of the ITO substrate has to be lowered in order to extract electrons. Cs_2CO_3 is one of the candidates for decreasing the work function by either spin coating or vacuum deposition. Upon annealing, the carbonate part desorbs and the metallic Cs produces substrate electrons, forming an interfacial dipole that is responsible for reducing the work function [106]. In 2012, the insulating polymers poly(ethylene imine ethoxylated) (PEIE) and poly(ethylene imine) (PEI) were found to be versatile for producing low-work function electrodes that can be used in OLEDs, OSCs, and OFETs [29]. The origin of the decrease in work function was attributed to the formation of a local dipole on the substrate surface, as suggested by density functional theory calculations. However, the volatile ethyleneimine dimer or trimer impurities contained in the PEI water solution were also found to act as *n*-dopant (electron dopant) for the electrodes, and the resulting interfacial dipole decreased the effective work function [107]. For the hole-extracting electrode in an inverted OSC, one must pay attention to atomic and/or molecular diffusion of buffer materials such as MoO_3 into the

organic layers [108, 109]. This diffusion increases the magnitude of electron transfer from the strong *p*-dopant MoO$_3$ to the organic molecules. Very recently, doped polymers have been used universally to control the substrate work function in the range of 3.0–5.8 eV [110]. Such a versatile method for producing the desired surface work function would enable the design of well-established interfaces.

Controlling the electrode work function in an OSC is very important for not only making electrode contacts ohmic but also for maximizing V_{oc}. The dependence of V_{oc} on the substrate work function has been measured [96], and it appears to be necessary that the donor HOMO and acceptor LUMO be pinned to the electrode Fermi levels in order to obtain the maximum V_{oc}.

10.4.2.2 Improvement of Physical Contact and Interface Morphology

The physical adhesion of the photoactive layer to the electrode surface is critical to sustaining the lifetime of an OSC and determining the charge-transfer kinetics at the electrode interfaces. So far, surface modification of a representative transparent electrode, ITO, has been examined. An ITO film is often fabricated on a glass substrate by sputter deposition followed by thermal annealing. This fabrication processes results in a highly polar surface with finite roughness and hydroxyl groups. As a result, the ITO surface has a surface energy of 60–70 mJ m^{-2}, which is much higher than that of an organic semiconductor film (10–50 mJ m^{-2}). Such a surface-energy difference leads to delamination of the organic semiconductor and consequently poor sustainability of the charge-transfer kinetics and thus the OSC performance [111]. An example of a surface modifier for ITO is phosphonic acid SAM that is functionalized with a fluorinated alkyl chain (Fig. 10.15) to tune the ITO surface work function, thereby decreasing the ITO surface energy and leading to long-term stability of the work function. An OSC based on this SAM demonstrated a longer lifetime [111]. For ZnO and AZO, alkaline hydroxide solution treatment was found to suppress the light-soaking effect, thereby leading to longer lifetimes of BHJ OSCs [112].

Another technique for changing the interfacial morphology is to use the nanostructure of the interfacial modifier. Nanorods of ZnO are now well established as a way to produce a large interfacial area at the electron-extracting electrode interface. In addition, PDMS stamps can increase the interfacial area. Both techniques contribute to increases in *FF* and J_{sc}.

10.4.3 Energetics and Charge Generation at Donor/Acceptor Interface

10.4.3.1 Energetics

Multilayered organic devices, both OSCs and OLEDs, encompass organic heterointerfaces whose function critically influences their performance. In particular,

evolution of the carrier transport levels (HOMO and LUMO) is essential for understanding the behavior of exciton and free carriers generated at the donor/acceptor interface. For example, any built-in potential near the interface can support the sweeping away of the photo-generated holes and electrons toward the respective electrode.

Together with metal/organic semiconductor interfaces, the energetics at organic heterointerfaces have been investigated by employing surface science techniques [88, 113, 114]. At this early stage of research, vacuum-level alignment appears to hold at most organic heterointerfaces because of van der Waals interaction at the interfaces. However, findings that show that the magnitude of the vacuum-level shift depends on the substrate work function [88, 113] and that electrons are injected through the bottom organic layer to the overlayer [86, 87] confirm the existence of a potential drop even at inert organic heterointerfaces. These studies advance the establishment of a comprehensive model for predicting the energy-level alignment at the interfaces.

Recently, it was found that the electrostatic model [84] (see Sect. 10.4.1) can describe the energy-level alignment at organic heterointerfaces [119] and that the simulation well reproduces the energy-level shift measured by UPS. Strongly motivated by the agreement between the simulations and experimental data, thorough theoretical simulations of energy-level alignment at all types of organic heterointerface have been carried out [115]. Figure 10.17 shows the simulated energy-level alignments for OSC-relevant donor/acceptor interfaces with various substrate work functions. As for the anode/donor/acceptor structure (Fig. 10.17a), when the substrate work function is high enough (cases for $E_F = 6.0$ and 7.0 eV), holes accumulate at the anode/donor interfaces because of the Fermi-level pinning, but no charges accumulate at the donor/acceptor interface; thus the potential drop is negligible. For the cathode/acceptor/donor structure (Fig. 10.17b), when the substrate work function is low enough (cases for $E_F = 3.0$ and 4.0 eV), the Fermi-level pinning again causes electron accumulation at the cathode/acceptor interface. Thus, the energy levels shift upward, whereas no potential change occurs at the donor/acceptor interface.

Poelking et al. demonstrated that the aggregated long-range quadrupole interaction is critical for obtaining the correct energetic landscape at an organic heterointerface [116, 117]. The electrostatic model is capable of including such an influence of the electrostatic potentials of π-conjugated molecules by considering the orientational dependence of the ionization energy and electron affinity.

The electrostatic model assumes the Frank-van der Merwe growth (layer-by-layer) of the respective organic film and therefore ideally sharp interfaces. However, at actual interfaces, intermixing [118] and molecular reorientation [119] may occur, thereby complicating the interfacial electronic structure. Actually, a phthalocyanine/fullerene interface, which is a prototypical donor/acceptor interface used in OSCs, tends to show an unusual potential distribution (Fig. 10.18a). This is independent of the types of substrate, phthalocyanine, and fullerene and of their thicknesses and evaporation speed during formation of the interface [103, 120]. The observed downward-and-then-upward shift has been interpreted as being caused
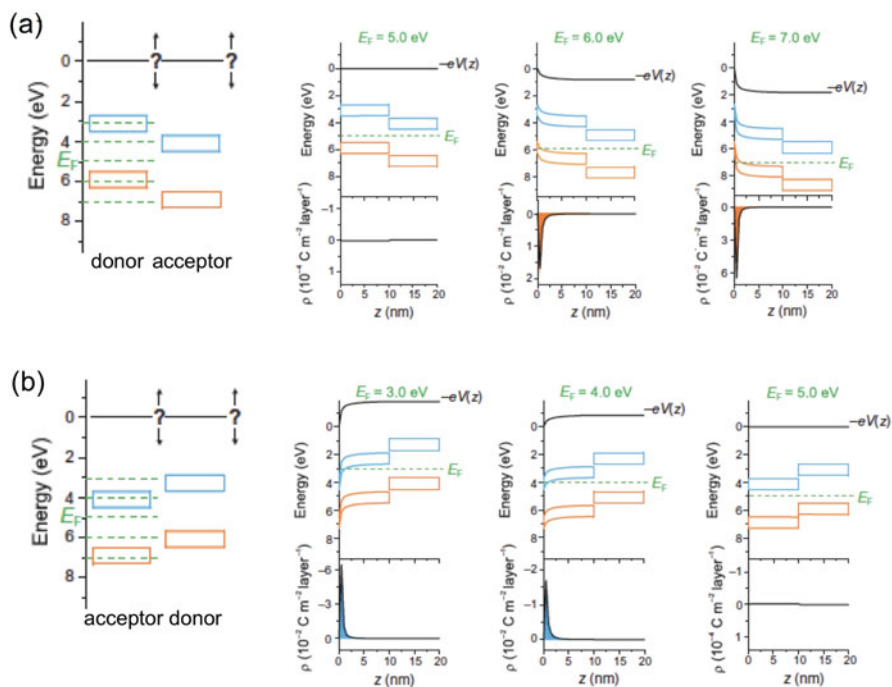
Fig. 10.17 Simulations of the energy-level alignment at donor/acceptor interfaces. (**a**) The very left panel shows the initial energies of the HOMO (orange rectangular) and LUMO (blue rectangular). The green-dashed lines correspond to the work function of the bottom substrates. The dependence of the simulation results on the electrode work function is shown in the second left to right panels. In each panel, the upper and lower plots illustrate the evolutions of the energies of the frontier orbitals and charge density as a function of the distance from a substrate surface (z), respectively. (**b**) Same for the reversed stacking sequence [115]

by an increase in the structural inhomogeneity in the phthalocyanine layers upon interfacial formation [120].

The energetic landscape across the donor/acceptor interface severely impacts the carrier generation and bimolecular recombination. The three-phase model was proposed to explain the widely observed efficient charge generation. The model assumes an amorphous mixed region between the pure donor and acceptor phases. In this amorphous region, the band gaps of the donor and acceptor increase because of shorter conjugation lengths. The existence of such a mixed region has been explored with UPS and cyclic voltammetry in the solid state [124].

An energy cascade designed by any method leads to an increase in free-carrier generation. The model in which the charge-transfer state and free carriers are in equilibrium predicts that more charges are generated in the donor and acceptor phases if an energy offset of 100 meV exists between the mixed and pure phases [52]. Actually, Izawa et al. confirmed that the energy cascade reduces bimolecular
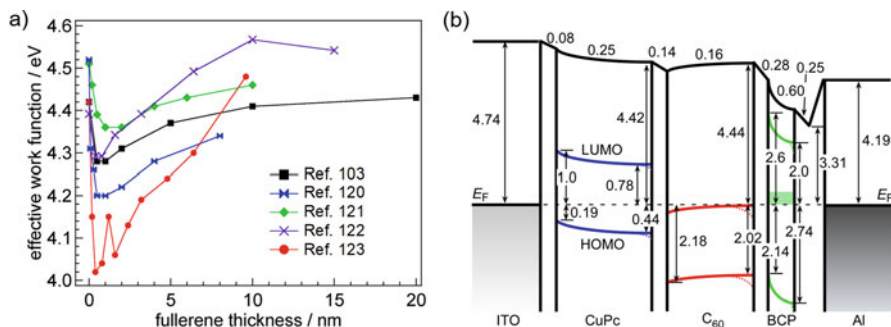
Fig. 10.18 (**a**) Downward-and-then-upward shift at phthalocyanine/fullerene interfaces. A dip in the vacuum level can be seen with increasing fullerene coverage [103, 120–123]. (**b**) Energy diagram of a planar heterojunction OSC determined by Kelvin probe (KP) measurements [103]. (Reprinted with permission from Ref. [103])

recombination at the donor/acceptor interface in the planar heterojunction OSC and increases FF and V_{oc} [125].

A more complicated issue is that the molecular orientation may change upon interface formation, which has been reported for a metal-free phthalocyanine/perfluorinated phthalocyanine interface [119]. Besides, chemical interaction in the solid phase can further alter the interfacial properties. The Diels-Alder reaction at a pentacene/C_{60} interface, which shows a PCE of ∼4% [47], can produce pentacene-C_{60} adducts [126]. Further investigation is necessary to elucidate the impact of the interface compound on OSC performance.

To reveal the full electronic structure of an OSC, several groups have analyzed the evolution of the vacuum-level and HOMO energies [103, 104, 127–129]. For a small-molecule-based OSC, a huge potential drop was observed at a C_{60}/BCP interface (Fig. 10.18b), which was attributed to the giant surface potential of BCP [103]. The measured shift would support efficient electron extraction toward the cathode. Davis et al. examined the electronic structure under ambient conditions using photoelectron yield spectroscopy and optical absorption spectroscopy [129]. Despite these measurements, a full picture of the energy and charge-density profiles remains elusive because surface science techniques can only probe up to ∼2 nm. Therefore, cross-sectional Kelvin probe (KP) measurements and simulation would help to deduce the complete energy diagram within an OSC, which would facilitate our understanding of carrier behavior in the device.

Utilization of the energy transfer across an organic heterostructure is also an important issue for enhancing device performance. As mentioned in Sect. 10.2.2, excitons diffuse to the donor/acceptor interface before recombination. The strategy is to use organic semiconductors that absorb different wavelengths and to transfer excitons to a specific donor/acceptor interface, which would lead to a significant improvement in J_{sc}. Figure 10.19 shows J-V curves and an energy diagram for 6 T/SubNc/subphthalocyanine (SubPc) OSC [130]. These three materials cover a wide range of the spectral distribution of sunlight. The important point is that
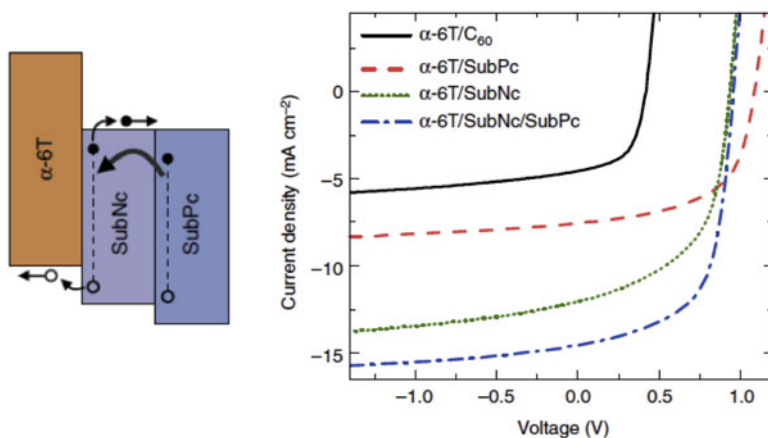
Fig. 10.19 Cascade energy transfer leads to high efficiency for a non-fullerene OSC. (Figures were reproduced with permission of Ref. [130])

because SubNc has a narrower band gap due to an extended π-conjugated ring, excitons generated in SubPc can transfer to SubNc. As a result, excitons generated in both the SubPc and SubNc layers are converted into free holes and electrons at the 6 T/SubNc interface. With this strategy, a PCE of 8.4% was achieved without a sole acceptor, namely, fullerene. This promising result paves a new way to harvest photons in the wide-ranged portion of the solar spectrum by controlling the energy structure.

10.4.3.2 Strategy to Enhance Free-Charge Generation

(a) *Increase of Average Distance of CT State*

As mentioned in Sect. 10.2, electrostatically bound CT states that form at the donor/acceptor interface can be a path to the CS state (free charges). For efficient photocurrent generation, the binding energy of the CT state (E_B) needs to be lowered. One strategy to reduce E_B is to increase the average distance between holes and electrons (r_{ct} in Eq. 10.7) [131–133]. Zhong et al. inserted an insulating wide-band-gap polymer, CYTOP, between P3HT and $PC_{61}BM$ in their planar heterojunction OSC. Insertion of CYTOP increased V_{oc} up to a thickness of 1 nm, while J_{sc} decreased concurrently with increasing thickness because of the reduced electron transfer between P3HT and $PC_{61}BM$ [131]. This decrease in J_{sc} was compensated by adding a dye into the CYTOP layer. This was attributed to more efficient exciton collection by energy transfer and charge separation with the charge cascade.

(b) *Molecular Orientation*

The molecular orientation at the donor/acceptor interface critically impacts the electronic coupling between the two materials and the degree of intermixing and thus the process of photocurrent generation. Rand et al. first suggested for a ZnPc/C_{60} bilayer OSC that the face-on orientation of ZnPc is favorable for photocurrent generation because of a larger electronic coupling between ZnPc and C_{60} [134]. However, it was also found from XPS and X-ray scattering studies that the degree of intermixing between ZnPc and C_{60} increased when ZnPc molecules were in the face-on orientation. This increased intermixing was attributed to higher J_{sc} than for its edge-on-oriented counterpart [135]. However, modifying the molecular orientation should also change the energy levels because the orientation of the molecular quadrupole determines the molecular surface potential [136], as well as the exciton diffusion and carrier mobility. Therefore, the impact of molecular orientation on photovoltaic performance is likely a diverse one.

(c) *Energy Cascade*

The equilibrium model for the CT state proposed by Burke et al. suggests that the energy cascade results in longer free-carrier lifetimes and a drastic increase in charge densities [52]. An energy offset of 100 meV in the HOMO and LUMO leads to tenfold increases in the charge densities in the donor and acceptor phases. Such an energy cascade is believed to exist in the interface between a polymer donor and a fullerene acceptor [124, 137]. The three-phase model assumes the formation of an amorphous mixed region between the aggregated donor and acceptor phases, in which the band gap of the polymer donor is larger than those of the pure phases. Analysis of UPS measurements on a polymer donor/C_{60} interface revealed that the HOMOs of the polymers donor shifted toward higher binding energies upon incremental deposition of C_{60}.

Izawa et al. reported extended carrier lifetimes and a higher charge density [125]. By combining contact film transfer and surface-segregated monolayer techniques, they designed an energy cascade and trap structure across a donor/acceptor interface. A PHJ OSC with an energy cascade could have an increased V_{oc} because of the elongated r_{ct} and a decreased bimolecular recombination because of the energy barrier. However, the lowest LUMO of the SSM layer in the system acts as recombination center for the trap-structured OSC. These results appear to correspond to the prediction made by Burke et al. [52]

(d) *Energy-Level Control of Quadrupole Potential*

Schwarze et al. reported recently that the ionization energy and electron affinity of organic donors such as ZnPc and SubPc can be controlled to 0.5–1.2 eV by mixing them with halogenated counterparts [138]. Concurrently, a ternary OSC with C_{60} as an acceptor shows V_{oc} variation when mixing ratio of the halogenated phthalocyanine varies. Such a new technology will provide optimal guidelines for producing efficient OSCs.

10.5   Summary and Outlook

This chapter has summarized the fundamental aspects of OSCs and given background knowledge on π-conjugated molecules and their interfacial properties. Newly synthesized polymer donors and (non-fullerene) acceptors will further increase the power-conversion efficiency of OSCs. However, economical and environmentally friendly methods of synthesis and device building should be explored simultaneously. Engineering long-ranged quadrupole interactions in organic semiconductors will open new designs for the photoactive layer. Besides, the use of electrostatic-potential models and the simulation of energy diagrams for OSC devices, including the impacts of the top electrode and light illumination, are required if we are to understand the carrier behavior within the device correctly and believably. By merging all these various streams of fundamental knowledge, we hope that optimal device design, based on both know-how and a bottom-up approach, will be possible in the near future.

References

1. E.C.R. Becquerel, Acad. Sci. **9**, 561–567 (1839)
2. D.M. Chapin, C.S. Fuller, G.L. Pearson, A new silicon p-n junction photocell for converting solar radiation into electrical power. J. Appl. Phys. **25**, 676 (2004). https://doi.org/10.1063/1.1721711
3. Solar Spectra: Air Mass Zero. Available at: http://rredc.nrel.gov/solar/spectra/am0/am0_index.html. Accessed 26 Dec 2016
4. L. Meng et al., Organic and solution-processed tandem solar cells with 17.3% efficiency. Science **361**, 1094 (2018). https://doi.org/10.1126/science.aat2612
5. R. Søndergaard, M. Hösel, D. Angmo, T.T. Larsen-Olsen, F.C. Krebs, Roll-to-roll fabrication of polymer solar cells. Mater. Today **15**, 36–49 (2012)
6. A. Pochettino, Acad. Lincei. Rendiconti. **15**, 355 (1906)
7. H. Inokuchi, Photoconductivity of the condensed polynuclear aromatic compounds. Bull. Chem. Soc. Jpn. **27**, 22–27 (1954)
8. H. Inokuchi, The discovery of organic semiconductors. Its light and shadow. Org. Electron. **7**, 62–76 (2006)
9. C.W. Tang, VanSlyke. Appl. Phys. Lett. **51**, 913 (1987)
10. J.H. Burroughes et al., Nature **347**, 539 (1990)
11. G.A. Chamberlain, Organic solar cells: A review. Sol. Cells **8**, 47–83 (1983)
12. Tang, C. W., Marchetti, A. P., Young, R. H. & Company, E. K. Organic photovoltaic elements. US Patent 4125414A. (1978)
13. Tang, C. W. & Company, E. K. Multilayer Organic Photovoltaic Elements. US Patent 4281053A. (1978)
14. C.W. Tang, Two-layer organic photovoltaic cell. Appl. Phys. Lett. **48**, 183–185 (1986)
15. R.F. Salzman et al., The effects of copper phthalocyanine purity on organic solar cell performance. Org. Electron. **6**, 242–246 (2005)
16. J. Wagner et al., Identification of different origins for s-shaped current voltage characteristics in planar heterojunction organic solar cells. J. Appl. Phys. **111**, 054509 (2012)
17. J.H. Bannock et al., The influence of polymer purification on the efficiency of poly(3-hexylthiophene): Fullerene organic solar cells. Sci. Rep. **6**, 23651 (2016)

18. M. Zhang, Irfan, H. Ding, Y. Gao, C.W. Tang, Organic Schottky barrier photovoltaic cells based on MoOx/C60. Appl. Phys. Lett. **96**, 183301 (2010)
19. F. Jin et al., Interface engineering of organic Schottky barrier solar cells and its application in enhancing performances of planar heterojunction solar cells. Sci. Rep. **6**, 26262 (2016)
20. C. Guo et al., Conjugated block copolymer photovoltaics with near 3% efficiency through microphase separation. Nano Lett. **13**, 2957–2963 (2013)
21. C. Grieco et al., Molecular rectification in conjugated block copolymer photovoltaics. J. Phys. Chem. C **120**, 6978–6988 (2016)
22. Y. Lin, X. Zhan, Non-fullerene acceptors for organic photovoltaics: An emerging horizon. Mater. Horiz. **1**, 470 (2014)
23. C.B. Nielsen, S. Holliday, H.-Y. Chen, S.J. Cryer, I. McCulloch, Non-fullerene Electron acceptors for use in organic solar cells. Acc. Chem. Res. **48**, 2803–2812 (2015)
24. C. Zhan, J. Yao, More than conformational "Twisting" or "Coplanarity": Molecular strategies for designing high-efficiency nonfullerene organic solar cells. Chem. Mater. **28**, 1948–1964 (2016)
25. G. Yu, J. Gao, J.C. Hummelen, F. Wudl, A.J. Heeger, Nature **270**, 1789 (1995)
26. J.M. Halls et al., Nature **376**, 498 (1995)
27. W. Zhao et al., Fullerene-free polymer solar cells with over 11% efficiency and excellent thermal stability. Adv. Mater. **28**, 4734–4739 (2016)
28. H.-H. Liao, L.-M. Chen, Z. Xu, G. Li, Y. Yang, Highly efficient inverted polymer solar cell by low temperature annealing of Cs_2CO_3 interlayer. Appl. Phys. Lett. **92**, 173303 (2008)
29. Y. Zhou et al., A universal method to produce low-work function electrodes for organic electronics. Science **336**, 327–332 (2012)
30. A. Orimo et al., Surface segregation at the aluminum interface of poly(3-hexylthiophene)/fullerene solar cells. Appl. Phys. Lett. **96**, 043305 (2010)
31. M.D. Clark, M.L. Jespersen, R.J. Patel, B.J. Leever, Predicting vertical phase segregation in polymer-fullerene bulk heterojunction solar cells by free energy analysis. ACS Appl. Mater. Interfaces **5**, 4799–4807 (2013)
32. J.-H. Huang et al., Fabrication of multilayer organic solar cells through a stamping technique. J. Mater. Chem. **19**, 4077 (2009)
33. B. Kippelen, J.-L. Brédas, Organic photovoltaics. Energy Environ. Sci. **2**, 251 (2009)
34. K. Nakano, K. Tajima, Organic planar heterojunctions: From models for interfaces in bulk heterojunctions to high-performance solar cells. Adv. Mater. **29**, 1603269 (2017)
35. R.R. Lunt, N.C. Giebink, A.A. Belak, J.B. Benziger, S.R. Forrest, Exciton diffusion lengths of organic semiconductor thin films measured by spectrally resolved photoluminescence quenching. J. Appl. Phys. **105**, 053711 (2009)
36. Y. Tamai, H. Ohkita, H. Benten, S. Ito, Exciton diffusion in conjugated polymers: From fundamental understanding to improvement in photovoltaic conversion efficiency. J. Phys. Chem. Lett. **6**, 3417–3428 (2015)
37. H. Najafov, B. Lee, Q. Zhou, L.C. Feldman, V. Podzorov, Observation of long-range exciton diffusion in highly ordered organic semiconductors. Nat. Mater. **9**, 938–943 (2010)
38. G. Grancini et al., Hot exciton dissociation in polymer solar cells. Nat. Mater. **12**, 29–33 (2012)
39. A.E. Jailaubekov et al., Hot charge-transfer excitons set the time limit for charge separation at donor/acceptor interfaces in organic photovoltaics. Nat. Mater. **12**, 66–73 (2012)
40. K. Vandewal et al., Efficient charge generation by relaxed charge-transfer states at organic interfaces. Nat. Mater. **13**, 63–68 (2013)
41. T.M. Clarke, J.R. Durrant, Charge photogeneration in organic solar cells. Chem. Rev. **110**, 6736–6767 (2010)
42. M.B. Smith, J. Michl, Singlet fission. Chem. Rev. **110**, 6891–6936 (2010)
43. J. Ma, K. Hashimoto, T. Koganezawa, K. Tajima, End-on orientation of semiconducting polymers in thin films induced by surface segregation of fluoroalkyl chains. J. Am. Chem. Soc. **135**, 9644–9647 (2013)

44. V.D. Mihailetchi, P.W.M. Blom, J.C. Hummelen, M.T. Rispens, Cathode dependence of the open-circuit voltage of polymer: Fullerene bulk heterojunction solar cells. J. Appl. Phys. **94**, 6849–6854 (2003)

45. B.P. Rand, D.P. Burk, S.R. Forrest, Offset energies at organic semiconductor heterojunctions and their influence on the open-circuit voltage of thin-film solar cells. Phys. Rev. B **75**, 115327 (2007)

46. C. Uhrich et al., Origin of open circuit voltage in planar and bulk heterojunction organic thin-film photovoltaics depending on doped transport layers. J. Appl. Phys. **104**, 043107 (2008)

47. W.J. Potscavage, A. Sharma, B. Kippelen, Critical interfaces in organic solar cells and their influence on the open-circuit voltage. Acc. Chem. Res. **42**, 1758–1767 (2009)

48. Wiley: Physics of Semiconductor Devices, 3rd Edition – Simon M. Sze, Kwok K. Ng. Available at: http://www.wiley.com/WileyCDA/WileyTitle/productCd-0471143235.html. Accessed 24 Jan 2017

49. H. Yoshida, Low-energy inverse photoemission study on the Electron affinities of fullerene derivatives for organic photovoltaic cells. J. Phys. Chem. C **118**, 24377–24382 (2014)

50. A. Wilke et al., Correlation between interface energetics and open circuit voltage in organic photovoltaic cells. Appl. Phys. Lett. **101**, 233301 (2012)

51. K. Vandewal, K. Tvingstedt, A. Gadisa, O. Inganäs, J.V. Manca, Relating the open-circuit voltage to interface molecular properties of donor: Acceptor bulk heterojunction solar cells. Phys. Rev. B **81**, 125204 (2010)

52. T.M. Burke, S. Sweetnam, K. Vandewal, M.D. McGehee, Beyond Langevin recombination: How equilibrium between free carriers and charge transfer states determines the open-circuit voltage of organic solar cells. Adv. Energy Mater. **5**, 1500123 (2015)

53. W. Tress et al., Imbalanced mobilities causing S-shaped IV curves in planar heterojunction organic solar cells. Appl. Phys. Lett. **98**, 063301 (2011)

54. J. Wagner et al., High fill factor and open circuit voltage in organic photovoltaic cells with diindenoperylene as donor material. Adv. Funct. Mater. **20**, 4295–4303 (2010)

55. M.M. Wienk et al., Efficient methano[70]fullerene/MDMO-PPV bulk heterojunction photovoltaic cells. Angew. Chem. Int. Ed. **42**, 3371–3375 (2003)

56. J.Y. Kim et al., Efficient tandem polymer solar cells fabricated by all-solution processing. Science **317**, 222–225 (2007)

57. S.E. Shaheen et al., 2.5% efficient organic plastic solar cells. Appl. Phys. Lett. **78**, 841–843 (2001)

58. S.H. Park et al., Bulk heterojunction solar cells with internal quantum efficiency approaching 100%. Nat. Photonics **3**, 297–302 (2009)

59. Z. He et al., Enhanced power-conversion efficiency in polymer solar cells using an inverted device structure. Nat. Photonics **6**, 593–597 (2012)

60. L. Dou et al., Tandem polymer solar cells featuring a spectrally matched low-bandgap polymer. Nat. Photonics **6**, 180–185 (2012)

61. X. Li et al., Dual plasmonic nanostructures for high performance inverted organic solar cells. Adv. Mater. **24**, 3046–3052 (2012)

62. K. Akaike et al., Ultraviolet photoelectron spectroscopy and inverse photoemission spectroscopy of [6,6]-phenyl-C_{61}-butyric acid methyl ester in gas and solid phases. J. Appl. Phys. **104**, 023710 (2008)

63. E.L. Ratcliff et al., Energy level alignment in PCDTBT:PC70BM solar cells: Solution processed NiOx for improved hole collection and efficiency. Org. Electron. **13**, 744–749 (2012)

64. L. Mattias Andersson, H. Tanaka, Empirical evidence for identical band gaps in substituted C_{60} and C_{70} based fullerenes. Appl. Phys. Lett. **104**, 043304 (2014)

65. R. Nakanishi, A. Nogimura, R. Eguchi, K. Kanai, Electronic structure of fullerene derivatives in organic photovoltaics. Org. Electron. **15**, 2912–2921 (2014)

66. K. Akaike, K. Kanai, Y. Ouchi, K. Seki, Side chain effect on electronic structure of spin-coated films of [6,6]-phenyl-C61-butyric acid methyl ester and its bis-adduct. Chem. Phys. **415**, 31–35 (2013)

67. C.-W. Chu, V. Shrotriya, G. Li, Y. Yang, Tuning acceptor energy level for efficient charge collection in copper-phthalocyanine-based organic solar cells. Appl. Phys. Lett. **88**, 153504 (2006)
68. M. Lenes et al., Fullerene bisadducts for enhanced open-circuit voltages and efficiencies in polymer solar cells. Adv. Mater. **20**, 2116–2119 (2008)
69. H. Sirringhaus, Integrated optoelectronic devices based on conjugated polymers. Science **280**, 1741–1744 (1998)
70. Z. Bao, A. Dodabalapur, A.J. Lovinger, Soluble and processable regioregular poly(3-hexylthiophene) for thin film field-effect transistor applications with high mobility. Appl. Phys. Lett. **69**, 4108–4110 (1996)
71. F.-C. Chen, H.-C. Tseng, C.-J. Ko, Solvent mixtures for improving device efficiency of polymer photovoltaic devices. Appl. Phys. Lett. **92**, 103316 (2008)
72. M.D. Irwin, D.B. Buchholz, A.W. Hains, R.P.H. Chang, T.J. Marks, p-Type semiconducting nickel oxide as an efficiency-enhancing anode interfacial layer in polymer bulk-heterojunction solar cells. Proc. Natl. Acad. Sci. **105**, 2783–2787 (2008)
73. T.-A. Chen, X. Wu, R.D. Rieke, Regiocontrolled synthesis of poly(3-alkylthiophenes) mediated by rieke zinc: Their characterization and solid-state properties. J. Am. Chem. Soc. **117**, 233–244 (1995)
74. T. Thurn-Albrecht, R. Thomann, T. Heinzel, S. Hugger, Semicrystalline morphology in thin films of poly(3-hexylthiophene). Colloid Polym. Sci. **282**, 932–938 (2004)
75. C. Yang, F.P. Orfino, S. Holdcroft, A phenomenological model for predicting thermochromism of regioregular and nonregioregular poly(3-alkylthiophenes). Macromolecules **29**, 6510–6517 (1996)
76. A. Tsumura, H. Fuchigami, H. Koezuka, Field-effect transistor with a conducting polymer film. Synth. Met. **41**, 1181–1184 (1991)
77. A. Zen et al., Effect of molecular weight and annealing of poly(3-hexylthiophene)s on the performance of organic field-effect transistors. Adv. Funct. Mater. **14**, 757–764 (2004)
78. R.J. Kline, M.D. McGehee, E.N. Kadnikova, J. Liu, J.M.J. Fréchet, Controlling the field-effect mobility of regioregular polythiophene by changing the molecular weight. Adv. Mater. **15**, 1519–1522 (2003)
79. K. Kanai et al., Effect of annealing on the electronic structure of poly(3-hexylthiophene) thin film. Phys. Chem. Chem. Phys. **12**, 273–282 (2010)
80. H. Wang et al., Band-bending in organic semiconductors: The role of alkali-halide interlayers. Adv. Mater. **26**, 925–930 (2014)
81. R.C. Shallcross et al., Quantifying the extent of contact doping at the Interface between high work function electrical contacts and poly(3-hexylthiophene) (P3HT). J. Phys. Chem. Lett. **6**, 1303–1309 (2015)
82. J. Niederhausen et al., Doping of C 60 (sub)monolayers by fermi-level pinning induced electron transfer. Phys. Rev. B **86**, 081411 (2012)
83. P. Amsalem et al., Role of charge transfer, dipole-dipole interactions, and electrostatics in fermi-level pinning at a molecular heterojunction on a metal surface. Phys. Rev. B **87**, 035440 (2013)
84. M. Oehzelt, N. Koch, G. Heimel, Organic semiconductor density of states controls the energy level alignment at electrode interfaces. Nat. Commun. **5**, 4174 (2014)
85. C. Tengstedt et al., Fermi-level pinning at conjugated polymer interfaces. Appl. Phys. Lett. **88**, 053502 (2006)
86. M.T. Greiner et al., Universal energy-level alignment of molecules on metal oxides. Nat. Mater. **11**, 76–81 (2011)
87. G. Ligorio, M.V. Nardi, C. Christodoulou, N. Koch, Organic semiconductor/gold interface interactions: From Physisorption on planar surfaces to chemical reactions with metal nanoparticles. ChemPhysChem **16**, 2602–2608 (2015)
88. J. Hwang, A. Wan, A. Kahn, Energetics of metal-organic interfaces: New experiments and assessment of the field. Mater. Sci. Eng. R Rep. **64**, 1–31 (2009)

89. L.-M. Chen, Z. Xu, Z. Hong, Y. Yang, Interface investigation and engineering – achieving high performance polymer photovoltaic devices. J. Mater. Chem. **20**, 2575 (2010)

90. R. Steim, F.R. Kogler, C.J. Brabec, Interface materials for organic solar cells. J. Mater. Chem. **20**, 2499 (2010)

91. G. Greczynski et al., Photoelectron spectroscopy of thin films of PEDOT-PSS conjugated polymer blend: A mini-review and some new results. J. Electron Spectrosc. Relat. Phenom. **121**, 1–17 (2001)

92. N. Koch, A. Vollmer, A. Elschner, Influence of water on the work function of conducting poly(3,4-ethylenedioxythiophene)/poly(styrenesulfonate). Appl. Phys. Lett. **90**, 043512 (2007)

93. T. Yamanari, T. Taima, J. Sakai, J. Tsukamoto, Y. Yoshida, Effect of buffer layers on stability of polymer-based organic solar cells. Jpn. J. Appl. Phys. **49**, 01AC02 (2010)

94. K. Kanai et al., Electronic structure of anode interface with molybdenum oxide buffer layer. Org. Electron. **11**, 188–194 (2010)

95. K.M. Knesting et al., ITO Interface modifiers can improve V_{OC} in polymer solar cells and suppress surface recombination. J. Phys. Chem. Lett. **4**, 4038–4044 (2013)

96. J. Wang et al., Effects of contact-induced doping on the behaviors of organic photovoltaic devices. Nano Lett. **15**, 7627–7632 (2015)

97. Z.R. Hong, C.J. Liang, X.Y. Sun, X.T. Zeng, Characterization of organic photovoltaic devices with indium-tin-oxide anode treated by plasma in various gases. J. Appl. Phys. **100**, 093711 (2006)

98. R.M. Cook et al., An electrode design rule for organic photovoltaics elucidated using molecular Nanolayers. Adv. Energy Mater. **1**, 440–447 (2011)

99. M. Vogel, S. Doka, C. Breyer, M.C. Lux-Steiner, K. Fostiropoulos, On the function of a bathocuproine buffer layer in organic photovoltaic cells. Appl. Phys. Lett. **89**, 163501 (2006)

100. H. Gommans et al., On the role of bathocuproine in organic photovoltaic cells. Adv. Funct. Mater. **18**, 3686–3691 (2008)

101. S. Toyoshima et al., Electronic structure of bathocuproine on metal studied by ultraviolet photoemission spectroscopy. Jpn. J. Appl. Phys. **46**, 2692 (2007)

102. S. Toyoshima et al., Ultraviolet photoemission study of interaction between bathocuproine and calcium. Jpn. J. Appl. Phys. **47**, 1397 (2008)

103. K. Akaike, Y. Kubozono, Correlation between energy level alignment and device performance in planar heterojunction organic photovoltaics. Org. Electron. **14**, 1–7 (2013)

104. Y. Nakayama et al., Complete demonstration of the valence electronic structure inside a practical organic solar cell probed by low energy photoemission. Adv. Energy Mater. **4**, 1301354 (2014)

105. S. Wang, T. Sakurai, R. Kuroda, K. Akimoto, Energy band bending induced charge accumulation at fullerene/bathocuproine heterojunction interface. Appl. Phys. Lett. **100**, 243301 (2012)

106. J. Huang, Z. Xu, Y. Yang, Low-work-function surface formed by solution-processed and thermally deposited nanoscale layers of cesium carbonate. Adv. Funct. Mater. **17**, 1966–1973 (2007)

107. S. Fabiano et al., Poly(ethylene imine) impurities induce n-doping reaction in organic (semi)conductors. Adv. Mater. **26**, 6000–6006 (2014)

108. Y. Nakayama et al., Origins of improved hole-injection efficiency by the deposition of MoO$_3$ on the polymeric semiconductor poly(dioctylfluorene- *alt* -benzothiadiazole). Adv. Funct. Mater. **19**, 3746–3752 (2009)

109. R.T. White, E.S. Thibau, Z.-H. Lu, Interface structure of MoO3 on organic semiconductors. Sci. Rep. **6**, 21109 (2016)

110. C.G. Tang et al., Doped polymer semiconductors with ultrahigh and ultralow work functions for ohmic contacts. Nature **539**, 536–540 (2016)

111. P.J. Hotchkiss et al., The modification of indium tin oxide with phosphonic acids: Mechanism of binding, tuning of surface properties, and potential for use in organic electronic applications. Acc. Chem. Res. **45**, 337–346 (2012)

112. H. Zhang et al., Overcoming electrode-induced losses in organic solar cells by tailoring a quasi-Ohmic contact to fullerenes via solution-processed alkali hydroxide layers. Adv. Energy Mater. **6**, 1502195 (2016)

113. S. Braun, W.R. Salaneck, M. Fahlman, Energy-level alignment at organic/metal and organic/organic interfaces. Adv. Mater. **21**, 1450–1472 (2009)

114. N.R. Armstrong et al., Organic/organic′ heterojunctions: Organic light emitting diodes and organic photovoltaic devices. Macromol. Rapid Commun. **30**, 717–731 (2009)

115. M. Oehzelt, K. Akaike, N. Koch, G. Heimel, Energy-level alignment at organic heterointerfaces. Sci. Adv. **1**, e1501127–e1501127 (2015)

116. C. Poelking et al., Impact of mesoscale order on open-circuit voltage in organic solar cells. Nat. Mater. **14**, 434–439 (2014)

117. C. Poelking, D. Andrienko, Design rules for organic donor-acceptor heterojunctions: Pathway for charge splitting and detrapping. J. Am. Chem. Soc. **137**, 6320–6326 (2015)

118. Y. Wakayama, D.G. de Oteyza, J.M. Garcia-Lastra, D.J. Mowbray, Solid-state reactions in binary molecular assemblies of F_{16} CuPc and Pentacene. ACS Nano **5**, 581–589 (2011)

119. A. Opitz et al., Organic heterojunctions: Contact-induced molecular reorientation, interface states, and charge re-distribution. Sci. Rep. **6**, 21291 (2016)

120. K. Akaike, N. Koch, G. Heimel, M. Oehzelt, The impact of disorder on the energy level alignment at molecular donor-acceptor interfaces. Adv. Mater. Interfaces **2**, 1500232 (2015)

121. Y.C. Zhou, Z.T. Liu, J.X. Tang, C.S. Lee, S.T. Lee, Substrate dependence of energy level alignment at the donor-acceptor interface in organic photovoltaic devices. J. Electron Spectrosc. Relat. Phenom. **174**, 35–39 (2009)

122. A. Wilke, T. Mizokuro, R.-P. Blum, J.P. Rabe, N. Koch, Electronic properties of Cu-Phthalocyanine/fullerene planar and bulk heterojunctions on PEDOT:PSS. IEEE J. Sel. Top. Quantum Electron. **16**, 1732–1737 (2010)

123. H.X. Wei et al., Electronic structures of planar and mixed C70/CuPc heterojunctions in organic photovoltaic devices. Org. Electron. **12**, 1422–1428 (2011)

124. S. Sweetnam et al., Characterization of the polymer energy landscape in polymer: Fullerene bulk heterojunctions with pure and mixed phases. J. Am. Chem. Soc. **136**, 14078–14088 (2014)

125. S. Izawa, K. Nakano, K. Suzuki, K. Hashimoto, K. Tajima, Dominant effects of first monolayer energetics at donor/acceptor interfaces on organic photovoltaics. Adv. Mater. **27**, 3025–3031 (2015)

126. T. Breuer, A. Karthäuser, G. Witte, Effects of molecular orientation in acceptor-donor interfaces between pentacene and C_{60} and diels-alder adduct formation at the molecular Interface. Adv. Mater. Interfaces **3**, 1500452 (2016)

127. J. Frisch et al., Full electronic structure across a polymer heterojunction solar cell. J. Mater. Chem. **22**, 4418 (2012)

128. A. Opitz, J. Frisch, R. Schlesinger, A. Wilke, N. Koch, Energy level alignment at interfaces in organic photovoltaic devices. J. Electron Spectrosc. Relat. Phenom. **190**, 12–24 (2013)

129. R.J. Davis et al., Determination of energy level alignment at interfaces of hybrid and organic solar cells under ambient environment. J. Mater. Chem. **21**, 1721–1729 (2011)

130. K. Cnops et al., 8.4% efficient fullerene-free organic solar cells exploiting long-range exciton energy transfer. Nat. Commun. **5**, 3406 (2014)

131. Y. Zhong, A. Tada, S. Izawa, K. Hashimoto, K. Tajima, Enhancement of V_{OC} without loss of J_{SC} in organic solar cells by modification of donor/acceptor interfaces. Adv. Energy Mater. **4**, 1301332 (2014)

132. D.M. Stevens, J.C. Speros, M.A. Hillmyer, C.D. Frisbie, Relationship between diode saturation current and open circuit voltage in poly(3-alkylthiophene) solar cells as a function of device architecture, processing conditions, and alkyl side chain length. J. Phys. Chem. C **115**, 20806–20816 (2011)

133. I.H. Campbell, B.K. Crone, Improving an organic photodiode by incorporating a tunnel barrier between the donor and acceptor layers. Appl. Phys. Lett. **101**, 023301 (2012)

134. B.P. Rand et al., The impact of molecular orientation on the photovoltaic properties of a Phthalocyanine/fullerene heterojunction. Adv. Funct. Mater. **22**, 2987–2995 (2012)
135. G.O. Ngongang Ndjawa et al., Impact of molecular orientation and spontaneous interfacial mixing on the performance of organic solar cells. Chem. Mater. **27**, 5597–5604 (2015)
136. S. Duhm et al., Orientation-dependent ionization energies and interface dipoles in ordered molecular assemblies. Nat. Mater. **7**, 326–332 (2008)
137. F.C. Jamieson et al., Fullerenecrystallisation as a key driver of charge separation in polymer/fullerene bulk heterojunction solar cells. Chem. Sci. **3**, 485–492 (2012)
138. M. Schwarze et al., Band structure engineering in organic semiconductors. Science **352**, 1446–1449 (2016)